RSC Applied Interfaces

ROYAL SOCIETY OF CHEMISTRY

PAPER

View Article Online
View Journal

Cite this: DOI: 10.1039/d6lf00026f

Taguchi optimised next-generation electric field assisted patterned poly-(vinylidene difluoride)-based hybrid nanogenerators and OmniGait-sensor

Vishnu N. Sasi, [a] Megha Garg, [a] P. Sravandas, [a] Shewli Pratihar, [a] Akash M. Chandran, [b] Arup R. Bhattacharyya [a] and Prasanna Kumar S. Mural *[a]

Received 29th January 2026,
Accepted 9th April 2026

DOI: 10.1039/d6lf00026f

rsc.li/RSCApplInter

The present study provides a Taguchi design of experiments (DoE) employed to optimise the near-field electric patterning (NFEP) process, enabling the fabrication of PVDF-based micropatterns for hybrid nanogenerator and OmniGait-sensor applications. Through this study, NFEP establishes an improved method that addresses the shortcomings of conventional electrospinning and advanced electric-field-assisted fabrication techniques. NFEP-driven surface engineering enhances the β-phase fraction in patterned PVDF, enabling the fabrication of well-defined structures with versatile designs. By optimising NFEP through Taguchi DoE and variance analysis, we achieved a robust process that drastically cuts time, energy, and resource consumption. Using NFEP, a diamond-mesh PVDF/barium titanate nanocomposite pattern was created. These patterns were employed as a piezoelectric and triboelectric layer, with PDMS as the counter tribo layer, to form a flexible hybrid piezo–tribo nanogenerator and sensor. By optimising the processing parameters using Taguchi DoE, the present work establishes a direct correlation between process optimisation and the fabrication of patterned polymer nanocomposites for nanogenerator and OmniGait sensor applications. This advancement improves versatility and opens new application horizons for nanogenerator and sensor technology.

Introduction

Electrospinning is one of the most promising methods for processing polymers using an electric field, due to its simplicity, low cost, and versatility,[1,2] making it highly attractive for applications in filtration, energy harvesting, microelectronics, biosensors, and tissue engineering.[3–5] Due to jet instability, the conventional electrospinning technique generates random nonwoven mats.[6] Moreover, it suffers from limitations, including solvent evaporation, random fibre orientation, and poor deposition control, which limit its use in precision-demanding fields.[4,7–9] Current deposition control techniques fail to achieve the precision required for nanogenerators and flexible electronics.[10,11] Globally, patterned structure-based devices are becoming integral in biomedical, energy, and sensor technologies.[12] Melt-based fused deposition modelling or optical-based lithographic techniques were used extensively to produce these patterned structures.[13–15] However, they lack the capacity to orient the dipole, which is necessary for nanogenerator applications. Integrating the electric field assistance with these techniques was also proposed to align the dipoles as required.[16–18] However, the fabrication processes typically require high energy inputs—such as heating for melting, powering lithography light sources, or applying strong electric fields for poling—making them energetically unsustainable. Hence, there is a pressing need for advanced electric-field-assisted strategies that enable controllable, site-specific, and accurate polymer deposition with high cost and energy efficiency.[19,20] Near-field electrospinning (NFES), introduced in 2006, has emerged as a powerful modification that minimises jet instability by reducing the nozzle–collector distance, enabling precise, aligned, and patterned polymer deposition onto a collector.[20–24] Previous efforts in NFES studies have primarily focused on improving the mechanical and structural properties of fibres, with comparatively limited attention to their functional applications.[11,25] The lack of targeted optimisation restricts the effective translation of NFES-fabricated structures into functional device platforms.[26]

Compared to all these electric field-assisted techniques, computer-aided design (CAD)-assisted near-field electric patterning (NFEP), derived from the fundamentals of NFES,

[a] Department of Metallurgical Engineering and Materials Science, Indian Institute of Technology Bombay, Mumbai, Maharashtra 400076, India.
E-mail: prasannamural@iitb.ac.in
[b] Department of Chemical Engineering, Maulana Azad National Institute of Technology, Bhopal, Madhya Pradesh 462003, India

was proposed as a micro-scale surface engineering technique in this work. NFEP offers a viable solution by enabling precise polymer deposition according to CAD specifications, without requiring costly lithography or melt-based methods, thereby aligning with the growing need for sustainable, accessible nano-energy manufacturing approaches.[22,26] Furthermore, the proposed technique represents a solution-based additive manufacturing strategy that facilitates dipolar orientation *via* an electric field and solvent evaporation, an inherently cost-free and well-established mechanism.[27–29]

To fully harness the potential, it is crucial to systematically optimise NFEP process parameters, which are often interdependent and sensitive to minor fluctuations. Conventional trial-and-error approaches require extensive time, energy, and resources, and fail to reveal the relative significance of each parameter. With its orthogonal array design, the Taguchi design of experiments (DoE) method provides an efficient statistical framework for evaluating multiple parameters simultaneously while minimising the number of experimental runs.[30,31] Complementarily, 'Analysis of Variance' (ANOVA) enables quantitative determination of each parameter's contribution and statistical significance, thereby identifying the most critical factors influencing the morphology, alignment, and deposition accuracy.[32,33]

Building on this foundation, the present study explores Taguchi design and ANOVA analysis to optimise the NFEP parameters, thereby establishing reliable control over patterning. Under optimised conditions, a patterned poly(vinylidene difluoride) (PVDF) polymer and composite were fabricated, and the performance of these patterns was systematically evaluated by fabricating a wearable contact–separation-based hybrid piezo–tribo nanogenerator (HPTNG) and an OmniGait sensor (OGS). A schematic illustration of the overall theme of this manuscript is shown in Fig. 1a. Over the years, various strategies have been employed to fabricate triboelectric nanogenerators and sensors for various applications, such as sleep monitoring,[34] human kinematic detections,[35,36] safety indicators,[37] *etc.* PVDF, owing to its excellent piezoelectric characteristics, and poly(dimethylsiloxane) (PDMS), a triboelectric elastomer, can be effectively integrated into wearable HPTNG and OGS systems. Given that human skin behaves as a highly tribopositive surface, contact motion between the skin and the PDMS layer can generate triboelectric charges. Meanwhile, mechanical

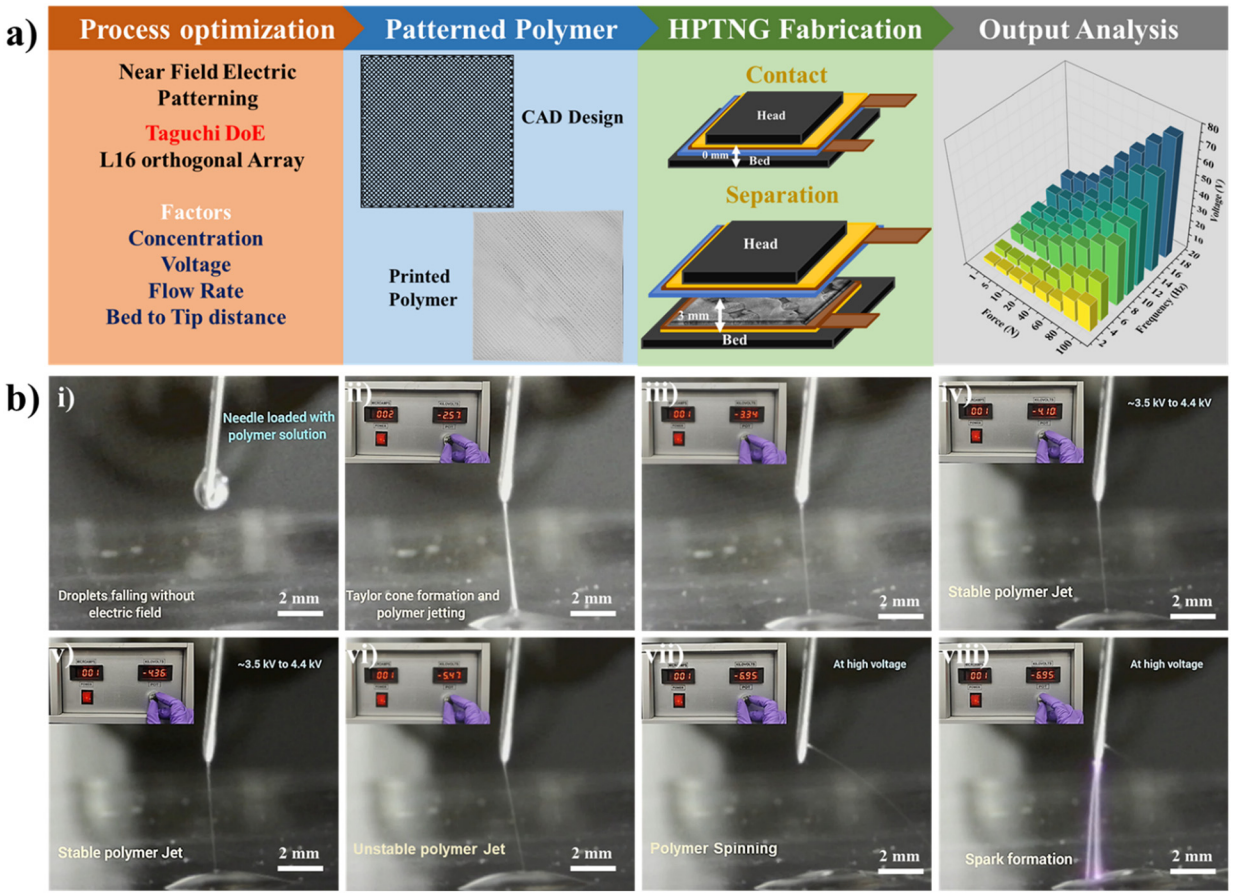

Fig. 1 (a) Schematic illustration showing the overall theme of the manuscript. (b) Near-field electrospinning process steps: (i) without an electric field; (ii) Taylor cone formation under an applied electric field; (iii–v) stable polymer jet formation within a voltage window of ~3.3 kV to ~4.4 kV; (vi) unstable polymer jet formation; (vii) electrospinning at high voltage; and (viii) spark formation at very high voltage.

deformation induced by human motion can simultaneously activate PVDF's piezoelectric response, enabling efficient conversion of biomechanical energy into electrical energy.

This study employs Taguchi DoE to optimise NFEP processing parameters, significantly improving functional performance and establishing a clear link between process control and device efficiency in nano-energy applications. Further, the present work highlights the effectiveness of Taguchi DoE for fabricating patterned polymer nanocomposites, enabling high-performance nanogenerators and OmniGait sensors.

Results and discussion

Optimisation of NFEP printing parameters

The printing parameters of NFEP are optimised using the Taguchi design of experiments and ANOVA. Preliminary experiments were done to identify the different levels of each factor considered for the optimisation.

Preliminary experimental results

Preliminary experimental trials were conducted to determine the printable levels of each factor. Among the possible output responses, the printed line width was selected as the primary

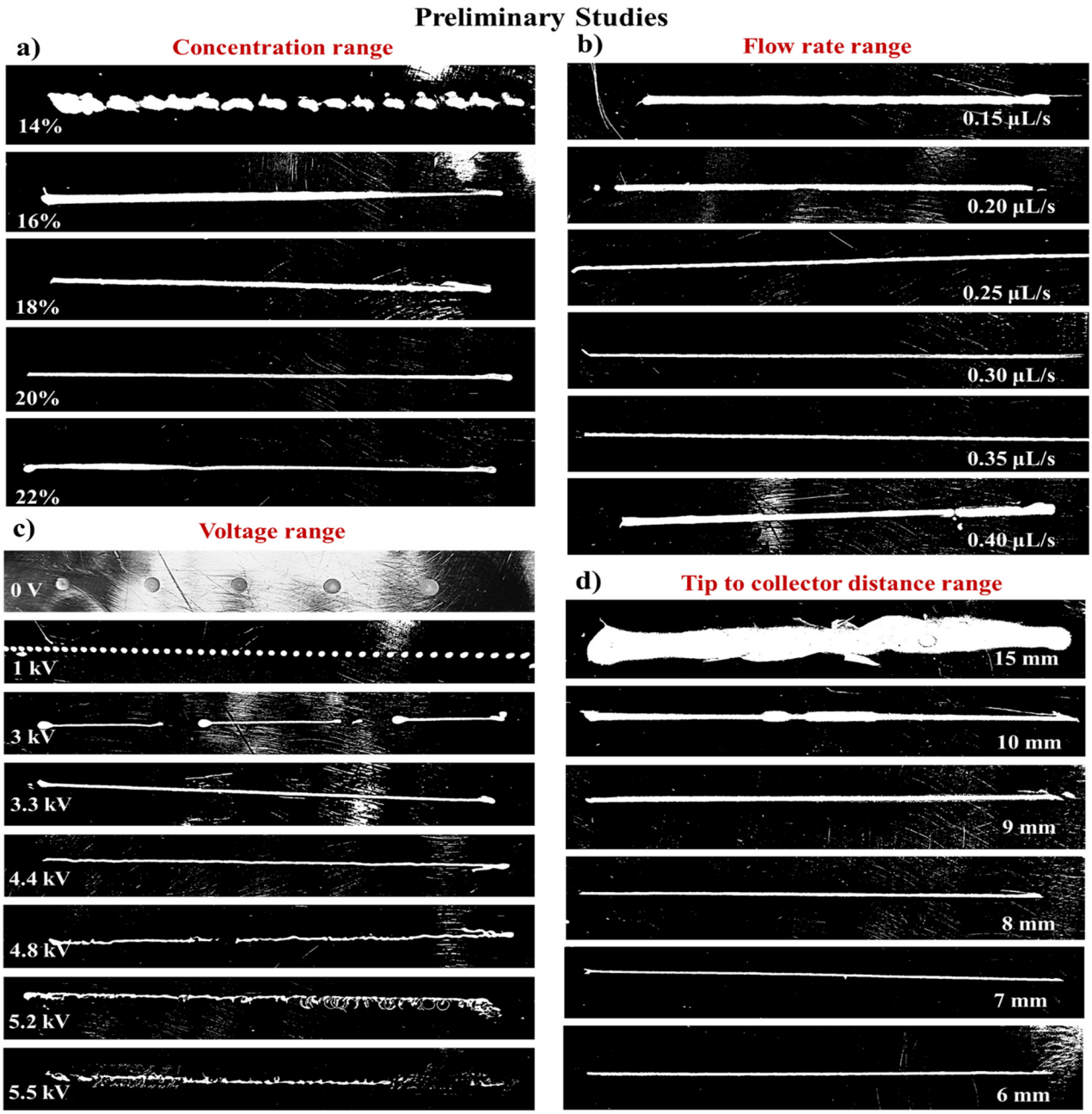

Fig. 2 Digital images illustrating the variation in the line profile with changes in the factors: (a) concentration, (b) flow rate, (c) voltage, and (d) tip to collector bed distance (all images are digitally contrast-enhanced for improved visualization without altering structural features).

response parameter because it directly reflects jet stability, electric field confinement, and solution stretchability in the near-field electrospinning process. Fig. 1b shows the behaviour of the polymer jet under an applied electric field. In the absence of an electric field, the polymer falls as a droplet, as shown in Fig. 1b(i). Upon applying an electric field, Taylor cone formation occurs, followed by the initiation of polymer jetting, as illustrated in Fig. 1b(ii). Achieving the minimum stable line width is essential for obtaining high-resolution patterns, which requires a stable jet, as shown in Fig. 1b(iii–v). As the applied voltage is further increased, the jet becomes unstable (Fig. 1b(vi)) and transitions into a whipping or spinning behaviour (Fig. 1b(vii)). At very high voltages, spark formation is observed (Fig. 1b(viii)), attributed to electrical breakdown of air. A SI video (Video S1) of the NFES process is also provided to further visualise the factors crucial for optimisation and pattern formation. Although Taguchi design and ANOVA optimisation were performed with line width as the primary response, this parameter inherently governs the fidelity and dimensional accuracy of more complex two-dimensional architectures, as shown in Video S1 and S2. Further, the optimised parameters were also tested for multi-line and grid printing to confirm pattern fidelity beyond single-line deposition.[38] Concentration, flow rate, tip-to-bed distance, and voltage were considered as the input parameters because they can strongly influence the NFEP process. Furthermore, changes in humidity and temperature can influence the solvent evaporation rate, charge dissipation, and jet behaviour. All experiments were conducted under ambient laboratory conditions of 25 ± 2 °C and 60 ± 5% relative humidity. The change in the profile of the line drawn with respect to the change in each factor is shown in Fig. 2. To identify the levels of concentration, different concentrations (14, 16, 18, 20, and 22 wt%) of PVDF solutions were employed by keeping a flow rate of 0.35 μL s^{-1}, a bed to tip distance of 7 mm and a voltage of 3.5 kV. The results in Fig. 2a show that the 14% PVDF concentration is not drawing the line correctly. The non-continuity in the polymer solution drawn from the needle under an applied electric field is clearly visible at a concentration of 14%. This implies that a sufficiently concentrated solution is necessary for the proper functioning of the NFEP process. The line was formed appreciably at the remaining concentrations (16, 18, 20, and 22 wt%), indicating better suitability for further analysis. A 20% concentrated PVDF solution was considered to optimise the flow rate. The bed-to-tip distance was maintained at 7 mm, and a 3.5 kV voltage was applied. The results of the flow rate range optimisation are presented in Fig. 2b. The results reveal that at both lower (0.15 μL s^{-1}) and higher (0.40 μL s^{-1}) flow rates, the line width was broader. At a lower flow rate, the insufficient supply of polymer solution leads to its interaction with the electric field, causing spreading due to the electrospinning or electrospraying process, and resulting in a broader line. However, at higher flow rates, the oversupply of polymer solution causes spreading after deposition, resulting in a thicker line.[39] This preliminary investigation suggests that flow rates of 0.20, 0.25, 0.30, and 0.35 μL s^{-1} can be considered as the levels for the flow rate factor. Fig. 2c shows the digital image of the line profile at varying voltages. For the voltage range optimisation, a 20 wt% PVDF solution was used, with a bed-to-tip distance of 6 mm and a flow rate of 0.35 μL s^{-1}. The results show that without an applied electric field, the PVDF solution does not form a continuous line but instead forms discrete droplets. As the voltage increases, the solution begins to be drawn from the syringe. Still, a stable, continuous line is achieved only at an optimal voltage of 3.3 kV and remains continuous up to 4.4 kV, as evident from Video S1. After that, the line began to spin and form a curly profile. This was due to the electrospinning process, which occurred at a higher voltage. Since the line was stable over 3.3–4.4 kV, the voltage levels were set to 3.5, 3.75, 4, and 4.25 kV. Both the lowest and highest ends of the optimal voltage range were deliberately excluded, as noise factors (temperature variation, humidity, or voltage fluctuations) at these margins may compromise the stability of the line profile. The tip-to-collector bed distance range was optimised using a 20 wt% PVDF solution at a flow rate of 0.30 μL s^{-1}. As the distance between the tip and the bed decreased, the minimum voltage required to draw a stable, continuous line decreased. Table S1 shows the voltage applied to form a continuous line as the bed-to-tip distance decreases. Moreover, as the distance decreased, a significant reduction in the width of the line was also observed, as shown in Fig. 2d. When the bed-to-tip distance was reduced below 6 mm, sparking and ignition of the polymer solution were observed under the applied voltage. Hence, distances of 6, 7, 8, and 9 mm were chosen as the factor levels for Taguchi optimisation.[40] In conclusion, concentration (16, 18, 20, and 22 wt%), flow rate (0.20, 0.25, 0.30, and 0.35 μL s^{-1}), voltage (3.5, 3.75, 4, and 4.25 kV), and bed to tip distance (6, 7, 8, and 9 mm) were considered as the factors and their levels are represented in Table 1.

Taguchi optimisation of NFEP through the S/N ratio approach. Experiments were conducted using the L16 orthogonal array design, as shown in Table S2.[41] All experiments were conducted in triplicate to account for variability and minimise the influence of experimental noise during the optimisation process. The line width was measured using digital vernier callipers with a least count of 0.01 mm, as shown in Fig. S1. A digital image of the results from the NFEP optimisation experiments for drawing a thinner line is presented in Fig. S2. The

Table 1 Factors, their levels, and assigned codes used in Taguchi optimisation of the NFEP process

Factors		Levels			
		1	2	3	4
Concentration (wt%)	A	16	18	20	22
Flow rate (μL s^{-1})	B	0.20	0.25	0.30	0.35
Bed to nozzle distance (mm)	C	6	7	8	9
Voltage (kV)	D	3.5	3.75	4	4.25

measurement results and calculated S/N ratios are presented in Table 2. Since obtaining the least width to the line drawn was considered as the output parameter, the S/N ratio was calculated using the 'smaller the better' approach of the Taguchi method.[42] The S/N ratio measurement enables the calculation of the variability of response due to different factors into a single performance matrix. After calculating the S/N ratio, the mean S/N at each factor level was measured to determine the average S/N at each level. For a given factor, the level corresponding to the highest mean S/N ratio is considered optimal, yielding the most robust performance against variability. Thereafter, the delta value of the level mean of S/N for all factors was calculated and ranked to identify the significance of each factor. A higher delta value for a factor indicates a greater difference between its maximum and minimum average responses across levels, signifying that the factor substantially influences the experimental output.[13,43] Table 3 presents the calculations of the level mean S/N ratio and the delta factor, and identifies the optimised parameters. The calculations suggest that 20 wt% of PVDF solution, a flow rate of 0.30 μL s^{-1}, a voltage of 3.5 kV, and a bed-to-tip distance of 6 mm will be the optimised parameters. Moreover, the delta calculation suggests that concentration is the most influential factor in determining the overall line width, followed by voltage and bed-to-tip distance, and finally by flow rate, which is the least significant.

ANOVA calculation. Furthermore, the percentage contributions of each factor and error were identified by examining their contributions to the total sum of squares. The equations used for the calculations are included in Section S1 of SI. The results align with the delta-factor measurement of the S/N ratio. However, a more precise contribution of each factor was obtained. ANOVA revealed that concentration was the dominant factor, accounting for 61.43% of the variation in width (Table 4).

The next most significant contribution was from voltage (18.90%) in the continuous line region, followed by bed-to-tip distance (12.71%), and least from flow rate (6.14%). Furthermore, the main effect plot of the mean S/N ratio at each level was constructed to graphically analyse the influence of the parameters, as shown in Fig. 3a. Later, a line was drawn using the optimised parameters with a pure PVDF solution, and the width was measured. It was found that when performing the experiment using the optimised parameters, the smallest width of 0.63 mm was obtained, as shown in Fig. 3b. A digital image illustrating the measurement of line width using a vernier calliper and the

Table 3 The level mean S/N ratio of each factor and the delta per factor are used to identify the optimised parameters

	Level means of S/N (η_j)	Delta per factor (max level mean S/N − min level mean S/N)	Best level (largest S/N)	Optimized parameters
A1	−11.03	9.51	A3	20 wt%
A2	−2.25			
A3	−1.52			
A4	−4.11			
B1	−5.99	2.70	B3	0.30 μL s^{-1}
B2	−5.81			
B3	−3.29			
B4	−3.83			
C1	−1.80	4.22	C1	6 mm
C2	−5.31			
C3	−5.78			
C4	−6.02			
D1	−1.65	5.05	D1	3.5 kV
D2	−3.97			
D3	−6.59			
D4	−6.70			
Mean ($\bar{\eta}$)	−4.73			

Table 2 Line width measurement results obtained from experiments based on the L16 orthogonal array design and S/N ratio calculation using the 'smaller the better' approach

	Input parameters				Output parameter (line width in mm)			η_i
Experiment no. (i)	Factor A	Factor B	Factor C	Factor D	Trial 1	Trial 2	Trial 3	S/N (dB, smaller the better)
I	1	1	1	1	2.10	2.15	2.05	−6.45
II	1	2	2	2	3.82	3.75	3.79	−11.57
III	1	3	3	3	3.99	4.04	4.02	−12.08
IV	1	4	4	4	5.01	5.09	4.99	−14.03
V	2	1	2	3	2.19	2.15	2.07	−6.60
VI	2	2	1	4	1.22	1.25	1.28	−1.94
VII	2	3	4	1	0.88	0.87	0.82	1.34
VIII	2	4	3	2	1.19	1.28	1.22	−1.80
IX	3	1	3	4	1.89	1.85	1.87	−5.44
X	3	2	4	3	1.99	1.95	1.99	−5.92
XI	3	3	1	2	0.72	0.69	0.72	2.97
XII	3	4	2	1	0.77	0.76	0.77	2.31
XIII	4	1	4	2	1.88	1.86	1.89	−5.47
XIV	4	2	3	1	1.59	1.51	1.55	−3.81
XV	4	3	2	4	1.81	1.85	1.91	−5.38
XVI	4	4	1	3	1.26	1.23	1.19	−1.78

Table 4 ANOVA measurement and identification of the percentage contribution from each factor

ANOVA table				
	Sum of squares (SS)	Mean square (MS)	MS/MS_{Error} (F)	% contribution
A	226.17	75.39	74.83	61.43
B	22.59	7.53	7.47	6.14
C	46.81	15.60	15.49	12.71
D	69.58	23.19	23.02	18.90
Total (SS_{Factor})	365.15	—	—	—
SS_{Total}	368.17			
SS_{Error}	3.02	1.01 (MS_{Error})		0.82
Total				100

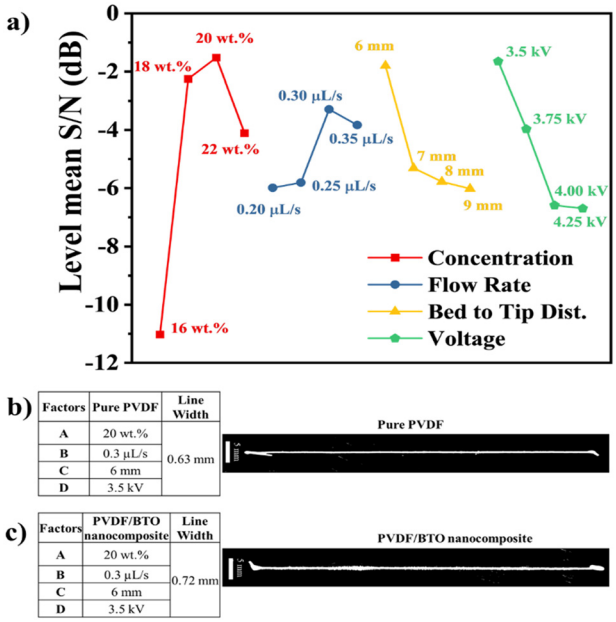

Fig. 3 Validation of Taguchi optimization. (a) ANOVA main effect plot of the level mean S/N ratio. (b) Line drawn using the optimized factors with pure PVDF solution. (c) Line drawn using the optimized factors with PVDF/BTO polymeric nanocomposite solution.

corresponding width achieved during NFEP at optimised parameters determined through Taguchi experiments is depicted in Fig. S1. This confirms that the chosen factors and levels were appropriate. Additionally, the width of a line drawn with PVDF containing 10% barium titanate (BTO) was measured. As shown in Fig. 3c, the results indicate a slight increase in line width, which may be attributed to differences in the specific gravity of the polymer nanocomposite solution compared to that of the pure PVDF solution. Table 5 presents a comparison between conventional electrospinning and optimised near-field electrospinning parameters. The results clearly indicate that near-field electrospinning is a more promising technique for reduced energy consumption and improved reproducibility.

Development of polymeric patterns using Taguchi optimised parameters

PVDF patterning. The NFEP process parameters have been optimised using the Taguchi experimental design. With these optimal parameters, the printing of a diamond mesh polymeric pattern was achieved using NFEP, as shown in Fig. 4. The CAD of the diamond mesh (Fig. 4a) pattern was created in Inkscape software and then printed using the Taguchi optimized parameters to obtain a PVDF polymeric pattern, as shown in Fig. 4b. The CAD design is chosen such that the stepper motor can achieve maximum precision in following the programmed path, without jerking or wobbling. A video demonstrating the NFES process is provided in the SI (Video S2).

Similarly, a few other patterns were also printed, as shown in Fig. S4, and the steps followed are included in Section S3. The printed patterns were dried under IR light for 1.5 h, as drying under IR light was found to be advantageous for obtaining a suitable pattern, as explained in Section S4 and depicted in Fig. S5. The SEM image of diamond mesh polymeric patterns of pure PVDF shows well-defined strokes and cavities, as evident in Fig. 4c. However, in some regions of the polymer composite-based pattern, a fibrous type of polymeric deposition is visible, as shown in Fig. 4d. This may be happening because of the difference in the specific gravity or the change in the conductivity of the solution due to the presence of filler, resulting in the spraying or spinning of the polymeric solution to a small extent. This can lead to

Table 5 Comparison between the near-field electrospinning and conventional electrospinning

Process	Applied voltage (kV)	Distance between the bed to tip (cm)	Precision	Fibre diameter	Material loss	Versatility	Remarks
Near field electrospinning	3–4	0.5–1	High (controlled deposition)	Micrometre	Less	High (various 2D architectures are possible)	This work
Conventional electrospinning	12–18	10–20	Low (random fibres)	Nanometre	High	Low (only the fibre mat will be obtained)	44, 45

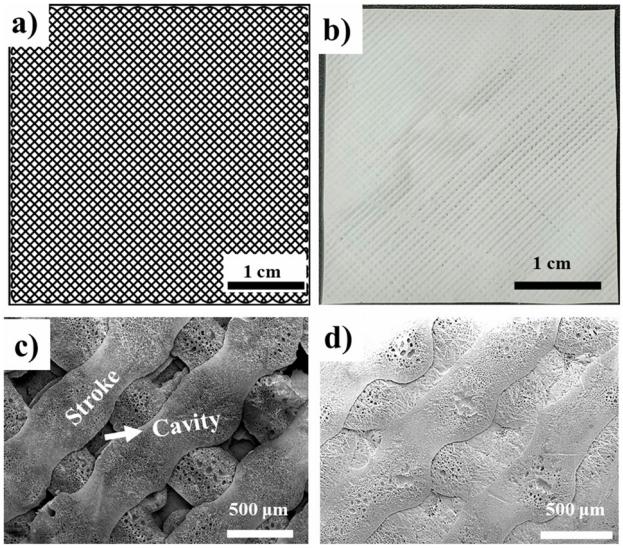

Fig. 4 Diamond mesh pattern of PVDF; (a) CAD design. (b) Digital image of the polymeric pattern of PVDF. (c) SEM image of the pure PVDF polymeric pattern. (d) SEM image of the PVDF/BTO patterned polymer composite.

an increased contact area during the fabrication of a contact–separation-based HPTNG, compared to pure PVDF with a 500 μm void microstructure.

Effect of filler on the pattern and surface roughness. Incorporation of the filler into the pure polymer alters the pattern profile and influences the surface morphology, which was already understood from Fig. 3c and 4d. Adding a filler into the polymer solution would change its specific gravity and conductivity, which can affect the flow rate and the behaviour of the solution under the electric field during the NFEP process. These changes significantly alter the surface profile of the line drawn using NFES and the resulting pattern, as evident in Fig. 5. The pattern printed with the pure polymer exhibits an excellent structure, with well-defined strokes and cavities. They had the microporosity and interconnected spherulitic structures of the PVDF matrix,[46,47] which can be identified in the magnified images of Fig. 5a–d. Energy-dispersive X-ray spectroscopy (EDS) spectra showing the presence of C and F, and corresponding elemental mapping of pure PVDF are shown in Fig. 5e and f. However, the addition of filler to PVDF led to structural changes. Furthermore, the cavities of the patterns appeared to be filled with polymer. This was not identified as an overflow of polymer, as shown in Fig. 5g. The SEM image of polymer overflow into the cavity is presented in Fig. S5b, and the observation in Fig. 5g is distinctly different from this. This behaviour may be attributed to electric spraying or spinning effects induced by the filler. These sprays or spins may account for the presence of fibrous or filamentous polymeric structures observed in the patterns' cavities. The high-magnification images in Fig. 5h, i, and j clearly show marginally smaller, interconnected spherulitic structures of PVDF. Uniform dispersion of nanoparticles on the polymer surface is also evident in the inset image of Fig. 5j, and the EDS spectra showing the presence of C, F, Ba, Ti, and O are depicted in Fig. 5k, along with the corresponding elemental mapping of the PVDF/BTO nanocomposite in Fig. 5l.

PVDF/BTO–PDMS hybrid nanogenerator and OmniGait sensor

A contact separation-based HPTNG and OGS were fabricated by placing a PDMS top layer and a PVDF/BTO bottom layer, separated by a distance of 3 mm, on a cyclic force generator instrument. The patterned polymers were named as follows: NEPV (near-field electric patterned pure PVDF), NEPV4BTO (4 wt% BTO in PVDF), NEPV6BTO (6 wt% BTO in PVDF), NEPV8BTO (8 wt% BTO in PVDF), and NEPV10BTO (10 wt% BTO in PVDF).

Material characterization. The X-ray diffraction (XRD) patterns in Fig. 6a confirm that the BTO particles were successfully retained in the polymer matrix without crystal distortion during the electric field-assisted patterning process. A prominent diffraction peak is observed at 2θ = 31.68° corresponding to the (110) plane in pure BTO and other composites (JCPDS no. #892475). The diffraction peaks located at 2θ = 22.36° (100), 31.68° (110), 39.03° (111), 45.31° (200), 51.09° (210), 56.34° (211), 66.18° (220), 70.50° (300), 74.96° (310), and 79.28° (311), consistently observed in all composites, clearly confirm the presence of perovskite-structured BTO in the polymer matrix.[48,49] However, a considerable reduction in the α peak (2θ = 18.56° of PVDF) was observed as the BTO nanofiller was added. This confirms the ability of BTO as a nucleating agent, because of the ferroelectric nature of BTO and its high dielectric constant,[50] which can reduce the energy barrier for nucleation.[51,52] Thus, their polar surfaces will interact with the PVDF matrix, leading to dipolar alignment of PVDF and thereby enhancing the β fraction.

Differential scanning calorimetry (DSC) was performed on all the patterned polymers to evaluate the bulk crystallinity of PVDF and its composites. Fig. 6b shows the second heating cycle, in which all the samples exhibit a melting temperature of ~163.7–163.9 °C. The percentage crystallinity (%X_c) was calculated using eqn (1), where φ is the weight fraction of the filler, ΔH_m is the melting enthalpy of the patterned polymer and its composites, and $\Delta H_{m(100)}$ is the melting enthalpy of 100% crystalline PVDF, taken as 104.5 J g^{-1}.[53,54]

$$\%X_c = \frac{\Delta H_m \times 100}{\Delta H_{m(100)}(1-\varphi)} \quad (1)$$

Fig. 6c shows the percentage crystallinity of the patterned PVDF and its composites. NEPV6BTO shows a maximum crystallinity of ~27.45% compared to the other samples. The melting enthalpy, calculated crystallinity, and melting temperature of the patterned polymers are summarised in Table S3 of the SI.

Fourier transform infrared spectroscopy (FTIR) was performed for BTO, unprocessed PVDF (PVDF Pellet), and all

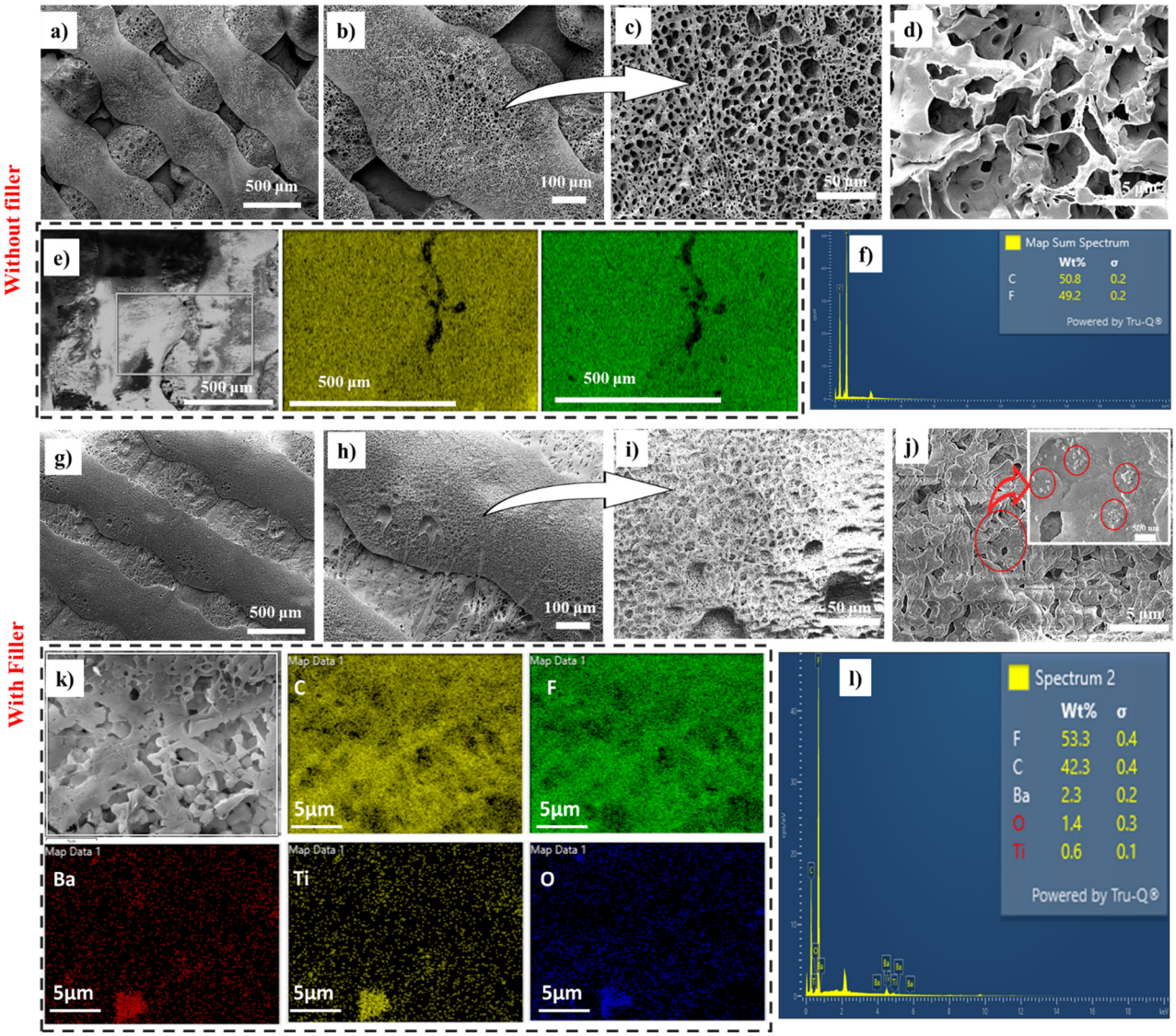

Fig. 5 SEM images of diamond mesh pure PVDF at different magnifications: (a) 60×, (b) 150×, (c) 500×, and (d) 5000×. (e) EDS spectra showing the presence of C and F, and (f) corresponding elemental mapping of pure PVDF. SEM images of the diamond mesh PVDF/BTO nanocomposite at different magnifications: (g) 60×, (h) 150×, (i) 500×, and (j) 5000× (inset image shows uniform dispersion of nanoparticles across the polymer surface). (k) EDS spectra confirming the presence of C, F, Ba, Ti, and O, and (l) corresponding elemental mapping of the PVDF/BTO nanocomposite.

electric patterned PVDF and its nanocomposites. Fig. 6d shows the FTIR spectra of BTO, pristine PVDF pellet, and other electrically patterned polymer nanocomposites. The BTO sample shows distinct carboxylic functional group peaks at 860 cm^{-1} and 1420 cm^{-1}. This may be attributed to residual impurities from the barium carbonate ($BaCO_3$) precursor. The broad absorption band below 700 cm^{-1} corresponds to Ti–O stretching vibrations of $BaTiO_3$.[55,56] The analysis of the polymer and its composites confirmed the presence of the characteristic vibrational modes of PVDF, enabling the evaluation of the effects of nanofillers and the applied electric field. The symmetric stretching and wagging vibrations of CF_2 were observed at ~1273 cm^{-1}, a distinctive feature of the β-phase. The peak at ~1234 cm^{-1} corresponds to CF_2 asymmetric stretching combined with CH_2 twisting, typically associated with the γ-phase. The in-plane bending/rocking of CF_2 at ~765 cm^{-1} is characteristic of the α-phase, while the strong band at 840 cm^{-1} confirms the formation of the electroactive β-phase. Additional peaks include the band at ~875 cm^{-1} and ~797 cm^{-1} (α-phase, CF_2 and CH_2 stretching), CH_2 twisting at ~971 cm^{-1} (α-phase), CF_2 stretching at ~1071 cm^{-1} and ~1177 cm^{-1} (β-phase), and the CH_2/CF_2 deformation band at ~1403 cm^{-1} (α-phase).

The coexistence of α, β, and γ phase markers indicates that the polymer contains mixed crystalline phases, with a clear enhancement of the electroactive β-phase in the presence of nanofillers and under the applied electric field.[57,58] Fig. 6e is a normalised [0, 1] FTIR absorbance spectrum of the electrically patterned polymer from ~700 cm^{-1} to ~850 cm^{-1}. The resulting graph clearly shows a decrease in the α fraction

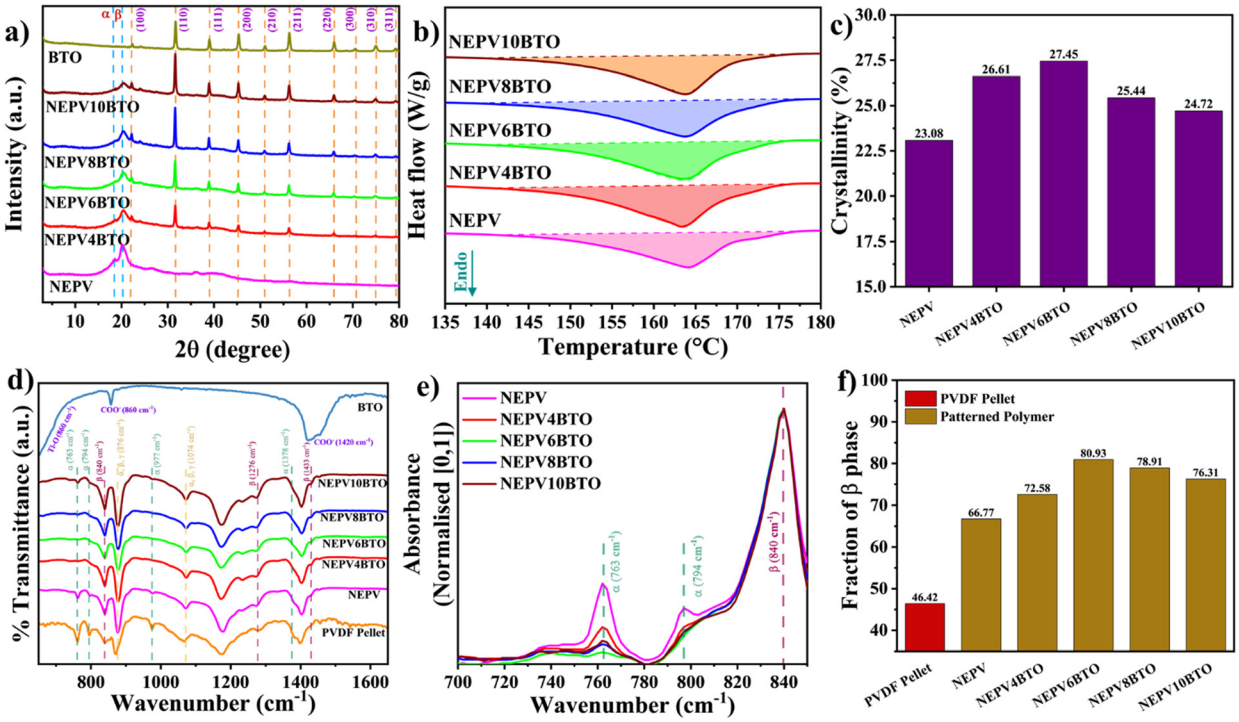

Fig. 6 Structural characterisation of patterned PVDF and its nanocomposites. (a) XRD patterns of pure BTO, NFEP-patterned PVDF, and PVDF/BTO composites with varying BTO loadings. (b) DSC thermograms of patterned PVDF and its nanocomposites. (c) Crystallinity of PVDF and its nanocomposites calculated from DSC. (d) FTIR spectra of PVDF and its composites. (e) Normalised (0–1) FTIR absorbance of electrically patterned polymers in the ~700–850 cm^{-1} wavenumber range. (f) Calculated β-phase fraction.

of PVDF with increasing nanofiller concentration, and the NEPV6BTO pattern shows the least α-phase fraction. The percentage β fraction (%$F(\beta)$) of the samples was calculated using eqn (2), where A_α – absorbance at ~765 cm^{-1}, A_β – absorbance at ~840 cm^{-1}, and the corresponding results are exhibited in Fig. 6f. The absorbance value of each composite at ~765 cm^{-1} and ~840 cm^{-1}, and the calculation steps are shown in Table S4.

$$\%F(\beta) = \frac{A_\beta \times 100}{(1.26 \times A_\alpha) + A_\beta} \quad (2)$$

The results show that the PVDF pellet, untreated with an electric field or with filler addition, had the lowest β fraction of ~46.42%. After electric field treatment of the PVDF, the %β fraction increased to ~66.77%. This was due to the dipolar alignment of the PVDF molecular chains along the electric field. Adding BTO to the polymer clearly increases the β fraction of the PVDF.[51,52] The maximum β fraction was achieved with the NEPV6BTO pattern at ~80.93% due to the greater nucleation induced by the BTO nanoparticles.[59] Moreover, the presence of a nucleating agent will protect the β-PVDF from reordering to its thermodynamically stable α phase.[60,61] Hence, the uniform dispersion of BTO nanoparticles is crucial for achieving the highest β-fraction. At higher BTO nanoparticle loading, nanoparticle agglomeration increases, limiting chain mobility and restricting chain orientation in the electric field. This is evident in the NEPV8BTO and NEPV10BTO patterned polymers. The β fraction was significantly reduced due to nanoparticle overloading.[44]

Furthermore, the morphology and nanoparticle dispersion of electrically patterned polymers were characterised by SEM. Fig. 7a shows the SEM image of BTO nanoparticles used in this study. The particle size distribution, analysed using ImageJ, exhibits a Gaussian distribution with an average particle size of ~65 nm, as illustrated in the inset image. The SEM image of NEPV6BTO is shown in Fig. 7b, characterised by clear strokes; however, the cavities are filled with the polymer. The strokes appeared completely rough, with an interconnected spherulite of PVDF, featuring pores present between the connections, as shown in Fig. 7c and e.[62] These pores may be formed during the solvent evaporation stage. Uniform dispersion of nanoparticles was also evident, as shown in the SEM images of Fig. 7c and d. The particle size distribution and average particle size of dispersed nanoparticles were calculated, and it was found that they showed similarity with the particle size distribution and average particle size of pristine BTO as shown in the inset image of Fig. 7c. Fig. 7f shows the presence of fibrous and filamentous polymer in the cavity of NEPV6BTO which occurred due to electrospraying or electrospinning, particularly when nanoparticles are involved. Agglomerated BTO nanoparticles were also observed in the cavity and on the surface, as shown in Fig. 7f and g, strongly suggesting that electrospraying was triggered by the narrowing of the

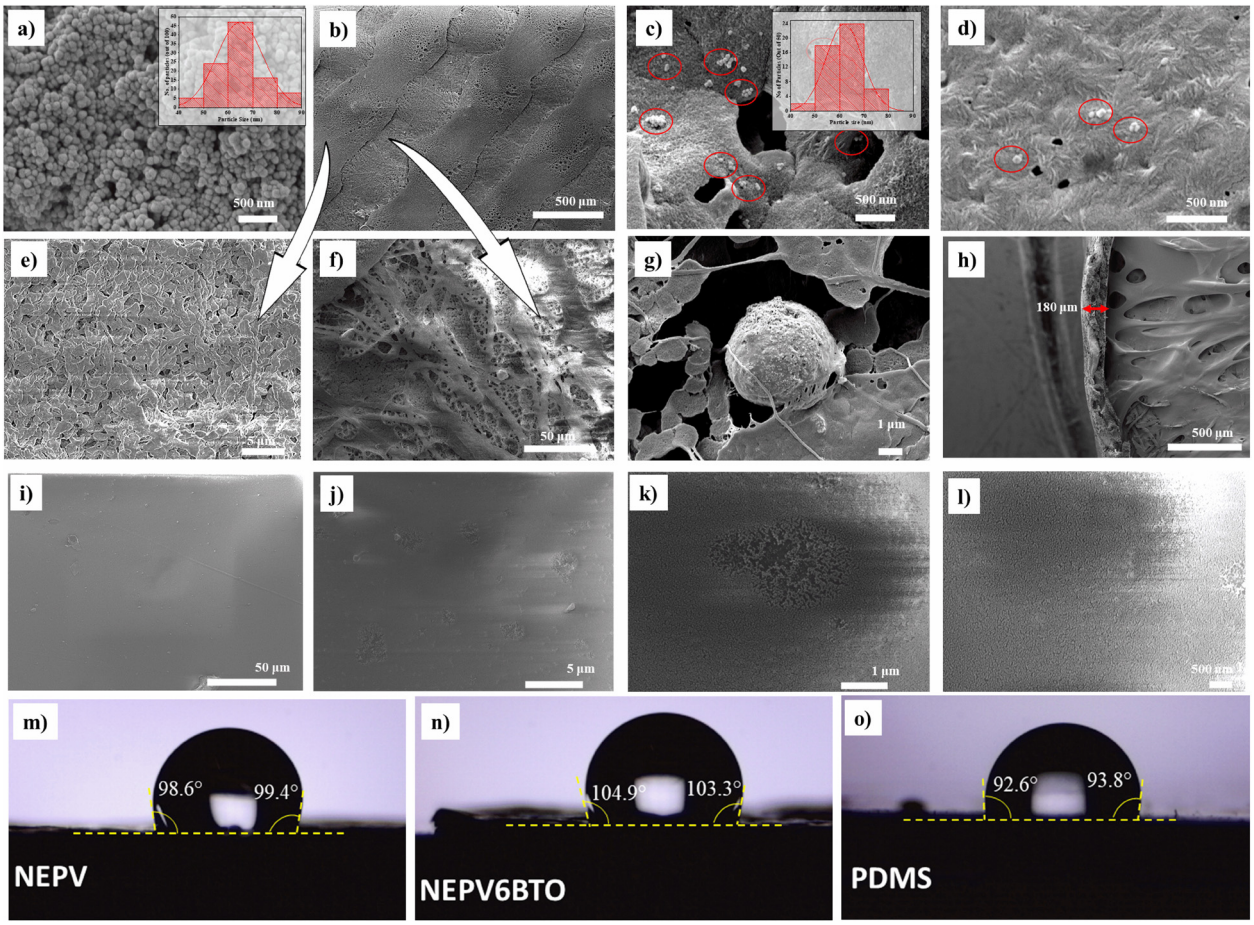

Fig. 7 SEM characterization of BTO nanoparticles and NEPV6BTO composite structures. (a) BTO nanoparticles with particle size distribution (inset). (b) Fabricated NEPV6BTO polymeric pattern. (c) Higher magnification image showing embedded BTO nanoparticles within the polymer matrix, with corresponding size distribution (inset). (d) Uniform nanoparticle dispersion in NEPV6BTO. (e) Stroke line morphology of the patterned structure. (f) Cavity features within the pattern. (g) Localized nanoparticle agglomeration within the cavity region. (h) Cross-sectional view indicating the thickness of the NEPV6BTO layer. SEM images of the PDMS surface at varying magnifications: (i) 500×, (j) 5000×, and (k and l) 20 000×. Contact angle measurements of (m) NEPV, (n) NEPV6BTO, and (o) PDMS, demonstrating surface wettability.

syringe needle in the NFES setup during the passage of these aggregated particles through the needle. The thickness of the NEPV patterns used in this study was ~180 μm, as clearly shown in the SEM cross-sectional image of NEPV6BTO in Fig. 7h. PDMS was used as the counter layer in the fabrication of the HPTNG and OGS. The PDMS exhibited a smooth surface morphology, as shown in Fig. 7i–l. However, slight surface roughness can be observed in Fig. 7k, which may have resulted from the removal of air bubbles during the vacuum-assisted curing process.

Contact angle measurements were performed to assess the hydrophobicity of the surfaces. PVDF, its nanocomposite, and PDMS exhibited hydrophobic behaviour, with contact angles greater than 90°. Fig. 7m shows that the contact angle of NEPV was approximately 99°, whereas the incorporation of BTO filler increased the hydrophobicity, resulting in a contact angle of approximately 104° (Fig. 7n). Incorporation of BTO enhances surface hydrophobicity, as evidenced by the increased contact angle, likely due to increased surface roughness and altered surface energy.[63,64] PDMS exhibited a contact angle of approximately 93° (Fig. 7o). The hydrophobicity of these layers facilitates improved charge retention and reduced moisture-induced dissipation, thereby enhancing the efficiency of contact–separation HPTNGs.[65]

The dielectric response in polymer–filler systems arises from several polarisation mechanisms, including dipolar, interfacial (Maxwell–Wagner–Sillars (MWS)), and space charge polarisation.[66] The frequency-dependent dielectric spectra from the broadband dielectric spectroscopy (BDS) of pure PVDF and PVDF/BTO nanocomposites (Fig. 8a–f) highlight how nanofiller loading influences dielectric permittivity, loss, AC electrical conductivity, electric loss modulus, and relaxation time. Higher dielectric constant (ε') values are observed at low frequencies due to interfacial polarisation and charge accumulation at the PVDF–nanoparticle interfaces.[67] With increasing frequency, dipoles cannot keep pace with the oscillating field, resulting in a decline in ε'. Among the nanocomposites, the NEPV6BTO sample exhibits

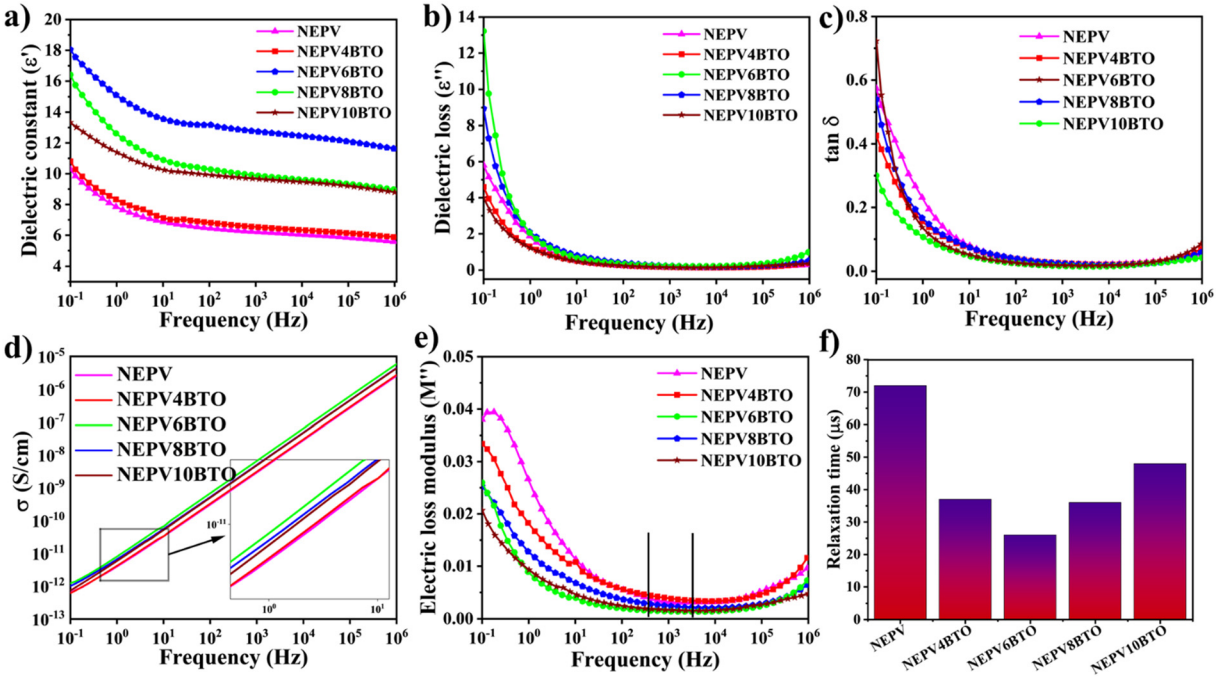

Fig. 8 Frequency-dependent BDS response of electrically patterned polymers: (a) real part of relative permittivity (ε'), (b) dielectric loss (ε''), (c) loss tangent ($\tan\delta$), (d) AC electrical conductivity, (e) imaginary part of electric modulus (M''), and (f) corresponding relaxation time, illustrating charge transport and polarization dynamics.

the maximum ε' of ~18, indicating strong interfacial polarisation, as shown in Fig. 8a. In contrast, higher loadings (8, 10 wt%) lead to a reduction due to nanofiller agglomeration and increased leakage paths. The dielectric loss (ε'') and $\tan\delta$ loss of pure PVDF (NEPV) and PVDF/BTO nanocomposites as a function of frequency are shown in Fig. 8b and c. For all the samples, the loss is higher in the low-frequency region due to space-charge polarisation and interfacial relaxation processes associated with the MWS effect, which provide sufficient time for charges to accumulate at the PVDF/BTO interfaces. Even though the dielectric loss is moderately high across all the samples, the output performance of the nanogenerator is predominantly governed by the effective polarisation. According to eqn (3), the polarisation (P) is directly proportional to the applied electric field (E) and the relative permittivity (ε') of the material, where ε_0 is the permittivity of free space and ε' is the relative permittivity.

$$P = \varepsilon_0(\varepsilon' - 1)E \quad (3)$$

An increase in ε' enhances the material's polarisation, leading to a higher induced surface charge density. This, in turn, improves the electromechanical coupling and charge generation capability of the nanogenerator.[68] As frequency increases, the loss decreases sharply because charge carriers can no longer follow the rapidly oscillating field, suppressing interfacial polarisation.[69] At higher frequencies, loss factors begin to rise for nanocomposites with higher nanofiller contents, especially NEPV6BTO and NEPV8BTO, reflecting the delayed dipolar relaxation of PVDF chains and intensified interfacial effects from well-dispersed nanoparticles. Notably, NEPV10BTO exhibits the highest dielectric loss at lower frequencies, which can be attributed to particle agglomeration and the formation of leakage pathways that enhance conduction losses.[70] In contrast, moderate nanofiller loadings (4–8 wt%) maintain relatively lower dielectric loss values across the frequency range, suggesting a better balance between interfacial polarisation and charge transport.[66,71] Fig. 8d shows the AC electrical conductivity (σ_{ac}) of pure PVDF and PVDF/BTO nanocomposites as a function of frequency. The results reveal that σ_{ac} decreases with decreasing frequency, reaching very low values at low frequencies. This reduction is desirable for dielectric applications, as lower electrical conductivity minimises leakage current and enhances the material's energy storage capability. With increasing frequency, σ_{ac} rises steadily due to hopping and tunnelling of charge carriers, following Jonscher's power law.[72] Among the nanocomposites, moderate nanofiller loading (such as 6 wt% BTO) exhibits improved electrical conductivity, resulting in enhanced electron transfer within the polymer matrix.[73] Fig. 8e shows the electric loss modulus as a function of frequency for the pure polymer and the corresponding nanocomposites. This represents the dielectric relaxation of dipoles within the nanocomposites. The relaxation peak at a higher frequency is attributed to the dipolar reorientation of PVDF.[46] This is calculated using eqn (4), where τ_{rel} is the relaxation time of the dipole and f is the frequency corresponding to the lowest electric loss modulus.[74]

$$\tau_{rel} = \frac{1}{2\pi f} \quad (4)$$

The calculated relaxation time is shown in Fig. 8f. The data suggest that the lowest relaxation time of ~26 μs is observed for the NEPV6BTO sample, which, in turn, requires the least time for dipolar reorientation, thereby minimising the loss effect at a critical frequency.

P–E loop measurement has been performed to evaluate the ferroelectric behaviour of the samples. The obtained P–E hysteresis loops clearly demonstrate the ferroelectric nature, as evidenced by the reversible polarisation under the applied electric field (see Section S5). The nearly symmetric loops indicate stable and reliable polarisation switching behaviour. With the incorporation of BTO nanofillers, an enhanced polarisation response is observed compared to the pure polymer (NEPV), as shown in Fig. S6a–c. This is evident from the increased loop area and higher remanent polarisation. The improvement can be attributed to the high dielectric constant and intrinsic ferroelectric nature of BTO, which promotes stronger dipole alignment and more efficient polarisation switching. Furthermore, the breakdown voltage increases from 1300 V for NEPV (Fig. S6a) to 1600 V for NEPV6BTO (Fig. S6b), indicating improved dielectric strength. This enhancement suggests better suppression of charge transport and reduced leakage pathways at optimal filler loading.

Kelvin probe force microscopy (KPFM) was employed to investigate the contact potential difference (CPD) and to estimate the surface work function of the samples. A gold-coated conductive AFM tip with a work function of ~5.1 eV (ϕ_{tip}) was used as the reference for the measurements. The surface work function of the sample (ϕ_{sample}) was calculated using eqn (5), where e is the charge of an electron, and V_{CPD} is the contact potential difference between the tip and the sample.[75]

$$\phi_{sample} = \phi_{tip} - eV_{CPD} \quad (5)$$

Fig. 9a shows the KPFM surface potential image of NEPV. The measured CPD is approximately ~−0.01 V, corresponding to a calculated work function of ~5.11 eV. The surface morphology analysis (Fig. 9b) reveals an RMS roughness of ~132 nm. Upon incorporation of BTO nanofiller, the CPD significantly increases to ~−0.44 V, resulting in an enhanced surface work function of ~5.54 eV, as shown in Fig. 9c. Additionally, the surface roughness increases to ~189 nm (Fig. 9d), indicating a more heterogeneous and textured surface. The reported surface work function value of PDMS was less than 5 eV.[76–78] Therefore, an increase in the work function of the PVDF nanocomposite enhances the work function difference between the triboelectric pair (PDMS–PVDF), leading to higher charge transfer, increased surface charge density, and improved HPTNG output performance.[77]

The ferroelectric domain switching behaviour and local piezoelectric properties of the optimised nanocomposite were investigated using piezo force microscopy (PFM) in contact mode. Fig. 9e shows the piezoelectric response strength of NEPV6BTO in a 5 μm × 5 μm area. The surface is characterised by remarkable roughness and heterogeneous regions, with brighter and darker areas. These distinct contrast regions confirm the spatial variation in piezoelectric activity, likely arising from filler distribution.[44,67] Fig. 9f illustrates the ferroelectric domain orientation of the material using different colour contrasts. Additionally, the direction of polarisation is indicated by a darker region (upward polarisation) and a brighter region (downward

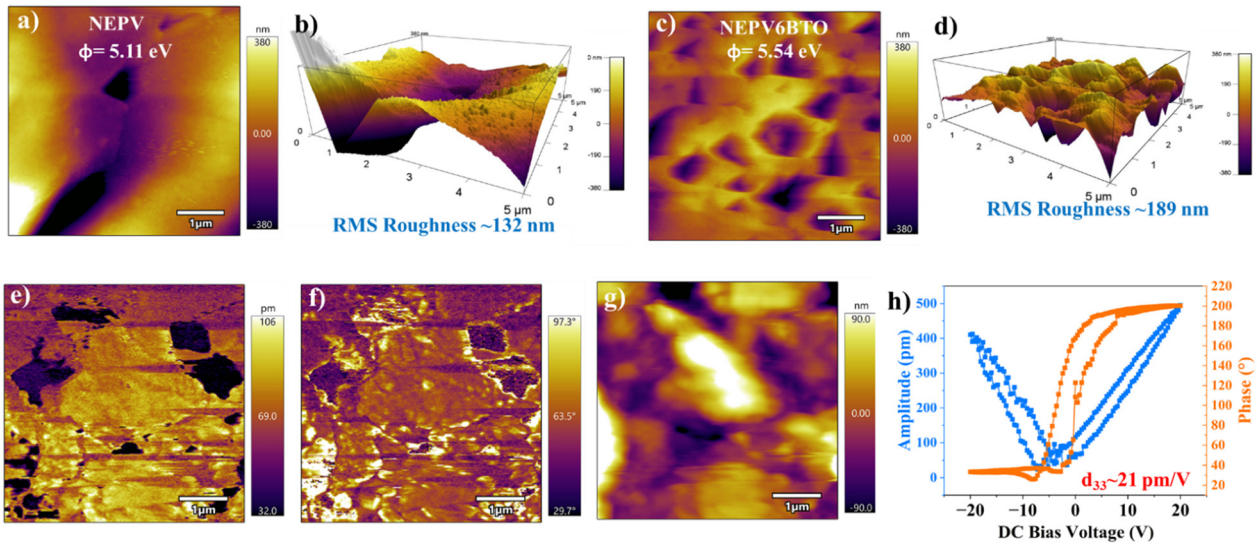

Fig. 9 AFM-based characterisation of piezoelectric and triboelectric properties. KPFM analysis includes (a) surface potential mapping of NEPV and (b) its corresponding 3D topography, along with (c) surface potential mapping of NEPV6BTO and (d) its corresponding 3D topography, highlighting variations in surface potential and roughness. PFM analysis of NEPV6BTO comprises (e) amplitude image, (f) phase image indicating domain orientation, (g) topography image, and (h) switching spectroscopy curves exhibiting characteristic butterfly and hysteresis loops, confirming piezoelectric and ferroelectric behaviour.

polarisation).[44] Fig. 9g represents the 2D surface morphology and topography of the sample, where the colour contrast indicates a relatively rough surface with significant height variations. Fig. 9h shows the amplitude and phase hysteresis curves for the NEPV6BTO nanocomposite. The curves illustrate the switching of ferroelectric domains upon the reversal of the electric field from negative to positive, confirming the material's ferroelectric behaviour.[79] Furthermore, the butterfly-shaped amplitude *vs.* bias voltage curve confirms the piezoelectric property of the NEPV6BTO sample, and the d_{33} value calculated from the slope of the butterfly curve was ~21 pm V^{-1}.

These results indicate that the incorporation of BTO nanofillers alters the surface work function, dielectric properties, and polarisation behaviour of the patterned PVDF while simultaneously enhancing its piezoelectric properties. The combined effects significantly improve the overall output performance, confirming that the fabricated device operates as a hybrid piezo–triboelectric nanogenerator.

Hybrid piezo–tribo nanogenerator performance evaluation. The contact–separation-based HPTNG device was fabricated by mounting the PDMS layer on the reciprocating head of the cyclic force generator and placing the electrically patterned PVDF and its nanocomposites on the stationary bed, as illustrated in Fig. 12d. The PDMS thickness was optimised, with 0.2 mm yielding the highest output, as shown in Fig. S7a. The force and frequency responses of all the samples were recorded using an oscilloscope. Fig. 10a and b present the open-circuit potential (OCP) and current responses of the patterns with varying nanofiller concentrations under an applied force of 10 N and a frequency of 10 Hz. The results indicate that the NFEP polymer nanocomposite containing 6 wt% BTO (NEPV6BTO) exhibits significantly enhanced OCP and current output. Specifically, NEPV6BTO achieved a peak-to-peak voltage of ~14 V (Fig. 10a) and a current of ~0.78 μA (Fig. 10b) measured across a 10 MΩ load resistance. Power density was evaluated by varying the external resistance, which revealed that the maximum power density occurs at 10 MΩ. The corresponding peak power density was calculated to be ~3.7 μW cm^{-2}, as shown in Fig. 10c. These findings clearly demonstrate that NEPV6BTO is the most effective composition for fabricating the PVDF/BTO–PDMS HPTNG device. Its superior performance is attributed to the highest β-phase fraction, enhanced crystallinity, and improved dielectric properties, as confirmed by FTIR, DSC, and BDS analyses. Additionally, PFM studies reveal its significant piezoelectric contribution, while KPFM measurements indicate an enhanced surface work function. Fig. 10d–f represent the voltage, current, and power density response output of the NEPV6BTO–PDMS HPTNG at different forces and frequencies. The result clearly shows an increase in the OCP as the force and frequency increase, reaching a maximum voltage of ~88.5 V, a current of ~4.8 μA, and a power density of ~66.8 μW cm^{-2} at 100 N and 20 Hz. Furthermore, the HPTNG's forward and reverse connection measurements yielded approximately the same peak-to-peak voltage output. The perfect reversal of polarity observed in Fig. 10g upon switching the connections confirms that the device exhibits no polarity loss or internal rectification.[80–82] The sensitivity, calculated from the slope of the pressure–voltage curve, varies with the operating frequency. A maximum sensitivity of 0.273 V kPa^{-1} was observed at a frequency of 20 Hz, as shown in Fig. 10h.[67] The charging–discharging capability of the HPTNG device is evaluated by charging and discharging different capacitors, as shown in Fig. 10i. The capacitors exhibit natural charging and discharging curves, and they are charged to ~4.1 V within seconds at a force of 100 N and a frequency of 20 Hz. Furthermore, the HPTNG devices demonstrated excellent cyclic stability at 50 N force and 20 Hz frequency, exhibiting only ~10% degradation over the initial 7500 cycles and maintaining consistent performance thereafter, with a stable OCP up to ~12 000 contact–separation cycles, as shown in Fig. 10j. The humidity study revealed that the device performs optimally under low-humidity conditions, delivering a maximum output of ~15.8 V at 20% relative humidity (RH) under an applied force of 10 N at 10 Hz. With increasing humidity, a gradual decrease in output was observed, with ~55% degradation in OCP at 100% RH, while still demonstrating reliable operation across a wide range of environmental conditions, as shown in Fig. 10k. Moreover, 23 LEDs glowed using the fabricated HPTNG, as evidenced in Fig. 10l and Video S3. The precise quantitative decoupling of piezoelectric and triboelectric contributions under identical dynamic operating conditions remains challenging. Therefore, the piezoelectric contribution to the overall hybrid output was evaluated by fabricating a dedicated piezoelectric device (Fig. S7b), as described in Section S6. The maximum voltage (Fig. S7c) and current (Fig. S7d) were ~7 V and ~0.4 μA, respectively, under an applied force of 100 N at 20 Hz. The clear peak reversibility observed upon switching the external connections confirms that the measured signal originates predominantly from the piezoelectric effect (Fig. S7e), with negligible contribution from triboelectric effects. Based on these results, the maximum possible piezoelectric contribution to the hybrid output is estimated at ~8%. Furthermore, the efficiency of the HPTNG was evaluated using a constant-force (impact) loading model. In this approach, a constant force of 100 N was assumed to act over the entire displacement.[83–85] Based on this model, the developed HPTNG exhibited a mechanical-to-electrical energy conversion efficiency of approximately 0.12%. The detailed calculation and explanation of this efficiency estimation are provided in Section S7 of the SI. The comparable results of the patterned PVDF-based HPTNG with the reported PVDF-based hybrid nanogenerator system, as presented in Table S5, suggest that the electrically patterned NEPV6BTO device is a promising candidate for efficient HPTNG fabrication.

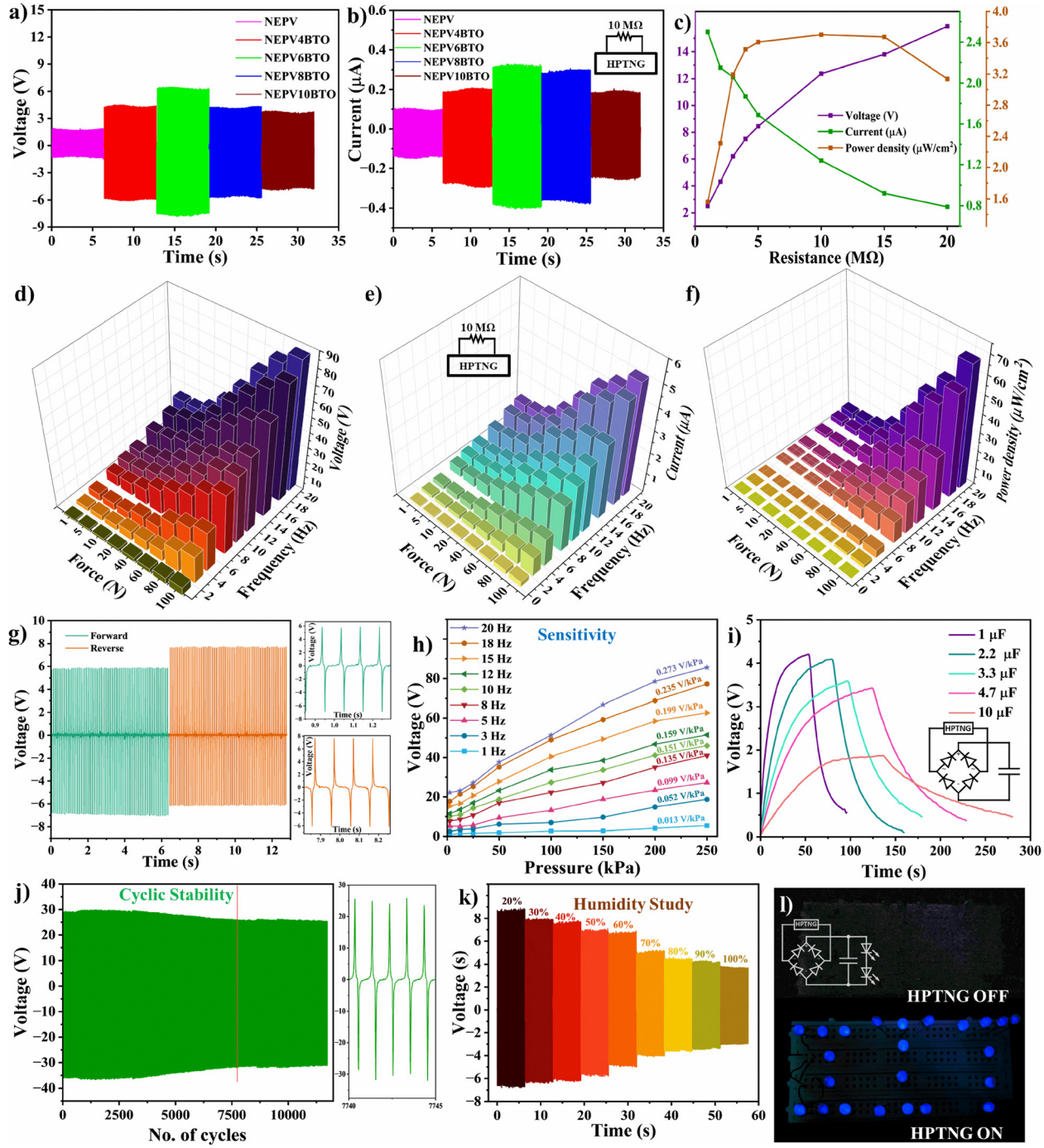

Fig. 10 HPTNG performance evaluation. (a) Output voltage of PVDF and PVDF/BTO composites with varying BTO loading; (b) corresponding output current; (c) power density of NEPV6BTO under different load resistances; (d–f) force–frequency response of NEPV6BTO showing (d) voltage, (e) current, and (f) power density; (g) output voltage under forward and reverse electrical connections; (h) sensitivity variation with frequency; (i) capacitor charging–discharging behaviour; (j) cyclic stability performance; (k) effect of humidity on device output; and (l) demonstration of powering 23 blue LEDs.

Real-time OmniGait motion sensing of human kinematics. A practical OGS device for human kinematics detection was fabricated by pasting the NEPV6BTO layer and PDMS layer on a PET sheet and separating them by a distance of 3 mm using double-sided tape, as shown in Fig. 11a. Different human kinematics were analysed and verified using the electrical signal and frequency of signals from these motions. Fig. 11 shows the distinct signals generated from various motion-like hand tapping (Fig. 11b), metacarpophalangeal (MCP) joint movement (Fig. 11c), proximal interphalangeal (PIP) joint motion (Fig. 11d), and the signal generated from the gait impact of the heel of the foot (Fig. 11e), toe of the

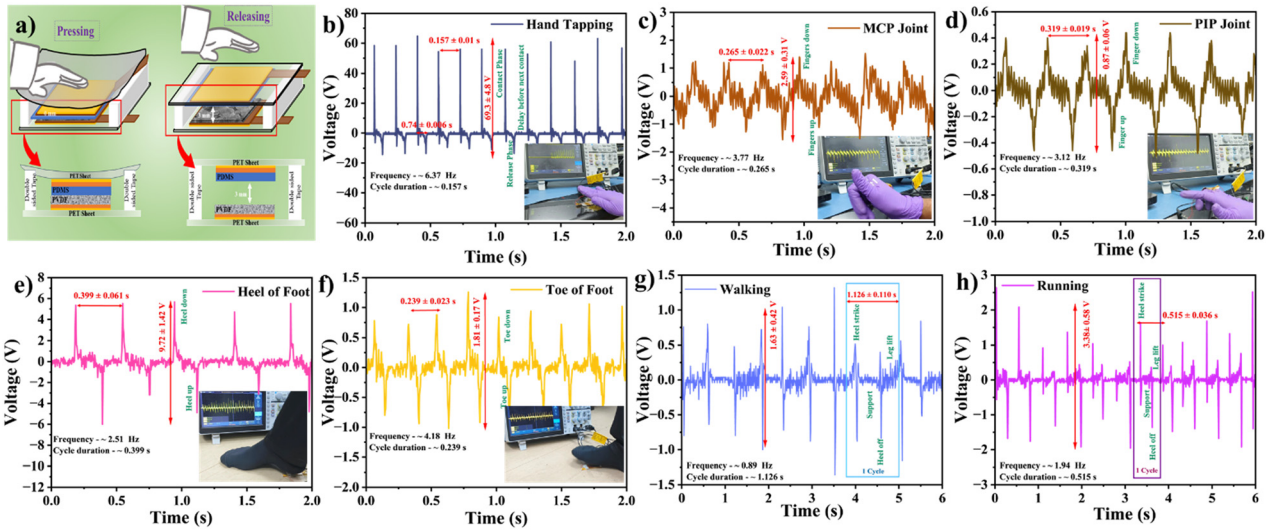

Fig. 11 (a) Schematic diagram of a practical OmniGait sensor fabricated using the NEPV6BTO polymer nanocomposite for human kinematic detection. Voltage response obtained from human motion, such as (b) hand tapping, (c) MCP joint movement, (d) PIP joint movement, (e) heel of the foot movement, (f) toe of the foot movement, (g) walking, and (h) running.

foot movement (Fig. 11f), walking (Fig. 11g) and running (Fig. 11h). Notably, walking and running exhibit distinct waveform characteristics: running shows higher frequency and larger peak amplitudes due to increased impact force and reduced cycle time, whereas walking produces relatively lower frequency and smoother signals. These differences demonstrate the device's ability to distinguish between gait patterns and indicate its potential for gait-phase identification and motion classification. Different motions produced distinct signal patterns, where variations in stride frequency, cycle duration, and peak-to-peak voltage output depended on the impact force and the specific motion pattern, as illustrated in Fig. 11. The distinct frequency and amplitude variations in the output signals enable differentiation between gait modes, highlighting the potential of the device for wearable gait recognition applications.

Conclusions

Inspired by near-field electrospinning, the present work demonstrated a near-field electric-patterning strategy to overcome the limitations of conventional electrospinning and other electric-field-assisted methods. The lack of targeted optimisation in the previous studies restricts the effective translation of NFES-fabricated structures into functional device platforms. Using a statistically robust Taguchi DoE and ANOVA enabled effective optimisation of the NFEP process. The study identified 20 wt% of PVDF concentration, 3.5 kV applied voltage, 0.30 μL s^{-1} flow rate, and a 6 mm tip-to-bed distance as the optimal parameters for achieving the finest printed lines. ANOVA confirms concentration as the dominant factor, followed by voltage, tip-to-bed distance, and flow rate. Using these optimised parameters, a diamond mesh-patterned PVDF nanocomposite-based active layer was fabricated and used in a BTO/PVDF–PDMS contact–separation-based HPTNG and OGS device. The nanocomposite containing 6 wt% BTO exhibited the highest β-phase content (~80.93%) as determined from FTIR analysis, along with enhanced crystallinity as evidenced by DSC, and a dielectric permittivity of ~18 obtained from BDS measurements. PFM analysis confirmed the piezoelectric response of the PVDF patterns, yielding a d_{33} value of ~21 pm V^{-1}. Furthermore, KPFM studies revealed that the incorporation of BTO nanofillers altered the surface potential. The nanocomposite HPTNG device containing 6 wt% BTO generated the highest peak-to-peak output voltage of ~88.5 V, an instantaneous power density of ~66.8 μW cm^{-2} and demonstrated an excellent cyclic stability of 12 000 cycles. The OmniGait sensor was fabricated and analysed, revealing distinct signal patterns in different human kinematics. Overall, the study demonstrates the effectiveness of the Taguchi design of experiments in optimising NFEP process parameters and fabricating patterned polymer nanocomposites to develop high-performance hybrid nanogenerator devices and OmniGait sensors.

Experimental

Materials and methods

For the optimisation of near-field electric patterning and fabrication of HPTNG and OGS, pure PVDF pellets of INOFLAR 1011 (weight average molecular weight, M_w = ~155 000 $gmol^{-1}$) received from Gujarat Fluorochemicals Limited were used. *N*,*N*-Dimethylformamide (DMF) from Merck was used as the solvent for preparing the polymeric solution, and barium titanate (BTO) nanoparticles (<100 nm, Sigma-Aldrich) were incorporated to form the nanocomposite. PDMS from the Sylgard 184 silicone elastomer kit was used as the top-

contacting layer material for fabricating the PVDF/BTO–PDMS nanogenerator. The copper (Cu) electrode used to fabricate the HPTNG was procured from ELK Tools (purchased *via* Amazon).

The crystal structure of the BTO nanoparticles and the corresponding PVDF-based nanocomposites was examined using an X-ray diffractometer (XRD) with Cu K_α radiation (λ = 1.542 Å) on a Rigaku diffractometer. The scans were recorded over a 2θ range of 3° to 80° at a scanning rate of 5° min^{-1}. Attenuated total reflectance Fourier transform infrared spectroscopy (ATR-FTIR) was employed to determine changes in the β-phase fraction of the samples. The measurements were carried out in the wavenumber range of 4000 cm^{-1} to 600 cm^{-1} using a Bruker Alpha II FTIR spectrometer. Surface morphology and EDS analyses of the samples were performed using a high-resolution field-emission scanning electron microscope (FEG-SEM, JEOL JSM-7600F) in dual-vacuum mode. Contact angle measurements were performed using a Data-Physics Instruments OCA 15SEC. The dielectric properties of PVDF and its nanocomposites were measured using broadband dielectric spectroscopy (BDS) (Novocontrol Concept 80). Films of 10 mm × 10 mm were prepared, coated with silver paste electrodes, and sandwiched before being loaded into the instrument. An AC voltage with an amplitude of 1 V was applied over a frequency range of 0.1 Hz to 10 MHz, and the corresponding dielectric data were recorded. Ferroelectric polarisation–electric field (P–E) hysteresis loops were recorded for 10 mm × 10 mm films using a TF Analyzer 2000 (aixACCT, Germany). Measurements were carried out at room temperature by applying triangular waveforms at 100 Hz under varying voltage conditions. Differential scanning calorimetry (DSC) measurements were carried out using a Rigaku DSC Vesta under a heating–cooling–heating–cooling cycle. The samples were heated from room temperature (RT) to 230 °C at a controlled heating and cooling of ~10 °C min^{-1} under a nitrogen atmosphere. The NFEP was performed using the Super ES1 near-field electrospinning instrument (Espin Nanotech, IIT Kanpur). A cyclic force generator (Holmarc, Kochi) was used for the characterisation of the force and frequency response of HPTNG, and a Tektronix TBS2072B oscilloscope with the P220 passive probe was used to capture the voltage output from HPTNG. Kelvin probe force microscopy (KPFM) and piezo-force microscopy (PFM) in contact mode were performed by using an Asylum Research MFP-3D BIO (USA) atomic force microscope with a gold-coated tip.

Optimisation of near-field electric patterning (NFEP) using the Taguchi method, S/N ratio, and ANOVA calculation

Systematic optimisation of experimental parameters is crucial for the development of any product. Using the Taguchi method, robust design can be systematically analysed using statistical methods. To improve product quality, engineers, industrialists, and academicians have extensively employed statistical methods such as signal-to-noise (S/N) ratio analysis, which assesses product performance by comparing signal variation to background noise, and ANOVA. Achieving a higher S/N ratio is crucial for any parameter to be resistant to its noise. Several factors must be controlled to optimise NFEP. Identification of these factors and their levels is the preliminary objective. To achieve the best patterning results, the line width drawn using the NFEP technique should be as narrow as possible. This section of the study focuses on optimising the width of a simple line drawn using NFEP. Width measurements of the line drawn were carried out using a vernier calliper, as shown in Fig. S1 of the SI.

Identification of factors, levels, and noise of the NFEP process

A continuous supply of a polymeric solution at the appropriate concentration and flow rate was sufficient to achieve the expected performance in the solution-based NFEP setup. Furthermore, since this is an electric field-assisted additive manufacturing strategy, the applied voltage and the bed-to-tip distance were also important. Therefore, the solution concentration, solution flow rate, syringe tip-to-collector distance, and voltage applied across the needle and collector were factors that could significantly influence NFEP output. In addition, the syringe needle diameter (60 μm), syringe diameter (7.8 mm), and stepper motor speed (500 mm min^{-1}) were kept constant. Uncontrollable variables, such as temperature (25 ± 3 °C), humidity (60 ± 5%), voltage fluctuations, marginal roughness, and non-uniformity in the depth profile of the collector bed at the micrometre scale, can cause noise and variations in the output.

PVDF solutions of different wt/wt% concentrations (14 wt%, 16 wt%, 18 wt%, 20 wt%, and 22 wt%) were prepared by dissolving an appropriate quantity of PVDF pellets in DMF solvent and stirring for 4 h at 60 °C. The solutions were then sonicated for 30 min to remove entrapped air bubbles. After cooling, the prepared solutions were loaded into the syringe and used to determine the effect of concentration on the line profile. Similarly, a 20 wt% PVDF solution was used to investigate the effects of voltage (0 to 5.5 kV), flow rate (0.15 to 0.40 μL s^{-1}), and tip-to-collector distance (6 to 15 mm) on process optimisation.

L16 orthogonal array and S/N ratio analysis

To optimise the NFEP using a Taguchi orthogonal array, the S/N ratio was calculated from data obtained from a four-level, four-factor design (L16) with three replications. Table S2 presents the coded L16 orthogonal array used to calculate the S/N ratio and to perform ANOVA. For the optimisation of an experiment with four factors, each at four levels, a total of 4^4 = 256 experimental runs would be required; however, the Taguchi design reduced the experiments to just 16 while still capturing the essential parameter interactions. Fig. S3 presents all 256 possible experiments necessary for complete optimisation. S/N ratio calculation is categorised into three

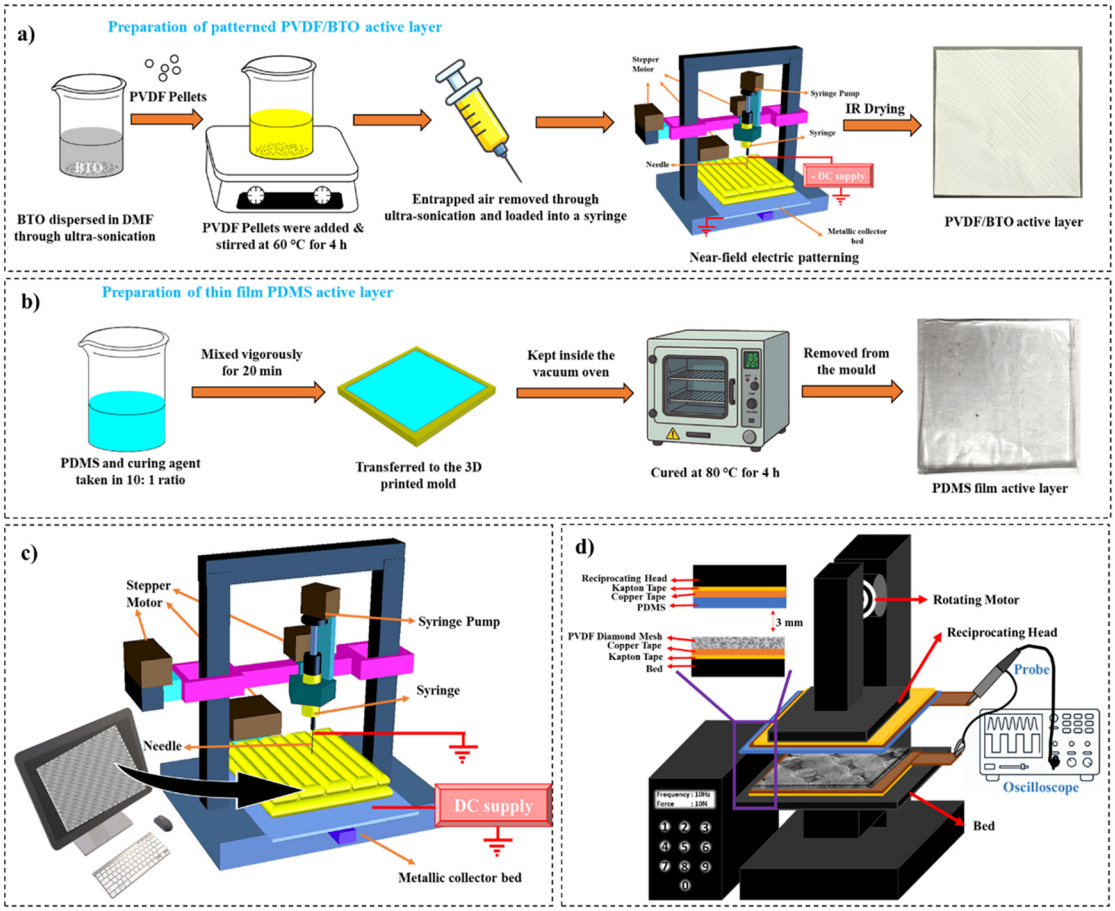

Fig. 12 Schematic illustration of the tribo-layer preparation and experimental setups. a) Preparation of the PVDF/BTO active layer through the NFEP process. b) Preparation of the thin film PDMS active layer. c) Schematic diagram of the NFEP setup. d) Cyclic force generator instrument and experimental setup created for characterizing the force-frequency response of the PVDF/BTO–PDMS HPTNG device.

approaches. Larger is better, smaller is better, and nominal is better. The selection of the appropriate Taguchi approach depends on the type of experiment. This study aimed to obtain the smallest possible line width; therefore, the 'smaller-is-the-better (STB)' criterion was adopted. The expression for calculating the S/N ratio using the "smaller the better" approach is shown in eqn (6), where S – signal, N – noise, dB – decibel, n – no. of trials, y_k – desired output at kth trial, and $\eta_i - \frac{S}{N}$ ratio for the ith experiment.

$$\frac{\text{Desired output}}{\text{Undesired variables}} = \frac{S}{N_{(\text{STB})}} = \eta_i(\text{in dB}) = -10\log\left(\frac{1}{n}\sum_{k=1}^{n} y_k^2\right) \quad (6)$$

Eqn (6) implies that, if the mean of the measurement output (y_k) is low, the mean of its square would also be low, resulting in a high S/N value. However, if the y_k is spread out to significant variance, the resulting sum of its squares would be high, causing the S/N to be smaller. ANOVA of S/N ratios was also performed to assess the statistical significance of the factors considered in the experiment. Moreover, ANOVA calculations provide insight into the contribution of each factor to the measurement variance.

Experimental setup for contact separation technique-based PVDF/BTO–PDMS HPTNG and OGS

Polymeric nanocomposites of PVDF and BTO were prepared with BTO weight fractions of 4, 6, 8, and 10 wt% relative to PVDF. The weight fractions of PVDF and BTO, along with the solvent quantity, are included in Table S2. The resulting solution was sonicated for 30 min to remove the entrapped air. After cooling, the solution was loaded into a 3 mL syringe and patterned using the NFEP setup with the optimal parameter set determined through the Taguchi design and the steps outlined in Section S2. The schematic illustration of the preparation of the PVDF/BTO patterned active layer is shown in Fig. 12a. Fig. 12c represents the schematic diagram of the NFEP setup. These polymeric nanocomposite patterns served as the one tribo layer; similarly, PDMS was used as another tribo layer in the fabricated HPTNG. A schematic illustration of the preparation of the PDMS film layer is shown in Fig. 12b.

A contact–separation-based HPTNG device (2 cm × 2 cm) was fabricated for force and frequency response characterisation. A cured PDMS film (2 cm × 2 cm) was used as the top triboelectric layer, to which a double-sided conductive Cu tape was attached as the electrode. The conductive acrylic adhesive ensured good electrical contact. A Kapton tape (polyimide sheet) was applied as an insulating layer, and the assembly was mounted on the reciprocating head of the cyclic force generator. Similarly, a 2 cm × 2 cm PVDF or PVDF/BTO nanocomposite film was used as the bottom layer, with a double-sided conductive Cu tape serving as the electrode. The adhesive side provided conductive contact, and Kapton tape was used as the insulating layer. This bottom assembly was fixed on a stationary platform. The conductive acrylic adhesive ensures uniform interfacial contact, minimising air gaps and interfacial resistance, thereby improving charge collection efficiency and reducing interface-related losses. The two layers were maintained at a separation distance of approximately 3 mm during operation. A schematic diagram of the cyclic force generator instrument and the experimental setup used for characterising force and frequency response is shown in Fig. 12d. The cyclic force generator can apply force (1–100 N) at various frequencies (1–20 Hz). The resulting HPTNG and NS device was connected to an oscilloscope using the P220 passive probe to collect the voltage output and perform other related measurements and studies.

Author contributions

Vishnu N. Sasi – data curation, investigation, methodology, writing – original draft, Megha Garg – writing – original draft, P. Sravandas – writing – review & editing, Shewli Pratihar – writing – review & editing, Akash M. Chandran – writing – review & editing, Arup R. Bhattacharyya – supervision, validation, Prasanna Kumar S. Mural – conceptualization, supervision, funding acquisition, validation.

Conflicts of interest

The authors declare no competing financial interests or personal relationships that could have influenced the work reported in this paper.

Data availability

The original contributions presented in the study are included in the article material and supplementary information (SI). Further inquiries can be directed to the corresponding authors.

Supplementary information: the SI associated with this study provides additional details supporting the main findings. It includes the method for developing patterned polymeric PVDF using NFEP, steps for ANOVA measurements, the development of different types of patterns, the effect of drying conditions on the pattern and surface, and further detailed analyses of the piezoelectric behaviour of NEPV6BTO and the optimisation of PDMS thickness. The supplementary data also include tables with coded L16 orthogonal array, the minimum voltage required to initiate continuous line drawing as a function of the tip-to-collector bed distance, crystallinity, and β-phase calculations, material composition, and comparisons with the existing literature. Additionally, supporting videos demonstrating the NFES process, patterning, device performance (LED illumination), and human motion-induced voltage responses are provided. See DOI: https://doi.org/10.1039/d6lf00026f.

Acknowledgements

The authors acknowledge the Indian Institute of Technology Bombay for providing the research facilities. We thank the Metallurgical Engineering and Materials Science Department at IIT Bombay for providing the laboratory facilities and the SEM and XRD central facilities. The authors acknowledge the central facility of the Chemistry Department, IIT Bombay, for providing the FTIR and DSC facility, and the BSBE Department, IIT Bombay, for providing the AFM facility. The authors acknowledge Gujarat Fluorochemicals Limited for providing the PVDF used in this research. The authors acknowledge the financial support from the Anusandhan National Research Foundation (ANRF), India (CRG/2023/000183 and EEQ/2018/000351).

References

1 D. R. Nisbet, J. S. Forsythe, W. Shen, D. I. Finkelstein and M. K. Horne, Review Paper: A Review of the Cellular Response on Electrospun Nanofibers for Tissue Engineering, *J. Biomater. Appl.*, 2008, **24**, 7–29.
2 C. Yang, Z. Jia, Z. Guan and L. Wang, Polyvinylidene fluoride membrane by novel electrospinning system for separator of Li-ion batteries, *J. Power Sources*, 2009, **189**, 716–720.
3 V. S. Reddy, Y. Tian, C. Zhang, Z. Ye, K. Roy, A. Chinnappan, S. Ramakrishna, W. Liu and R. Ghosh, A review on electrospun nanofibers based advanced applications: From health care to energy devices, *Polymers*, 2021, **13**, 3746.
4 D. Demir, N. Bolgen and A. Vaseashta, Electrospun Nanofibers for Biomedical, Sensing, and Energy Harvesting Functions, *Polymers*, 2023, **15**, 4253.
5 X. Chen, J. Wang, J. Zhang, H. Lin, M. Tian, M. Li and Y. Tian, Development and application of electrospun fiber-based multifunctional sensors, *Chem. Eng. J.*, 2024, **486**, 150204.
6 M. Ahmadi Bonakdar and D. Rodrigue, Electrospinning: Processes, Structures, and Materials, *Macromolecules*, 2024, **4**, 58–103.
7 A. Bin Rashid, M. Haque, S. M. M. Islam and K. M. R. Uddin Labib, Nanotechnology-enhanced fiber-reinforced polymer composites: Recent advancements on processing techniques and applications, *Heliyon*, 2024, **10**, e24692.
8 B. A. Venmathi Maran, S. Jeyachandran and M. Kimura, A Review on the Electrospinning of Polymer Nanofibers and Its Biomedical Applications, *J. Compos. Sci.*, 2024, **8**, 32.

9 J. Song, X. Lin, L. Y. Ee, S. F. Y. Li and M. Huang, A Review on Electrospinning as Versatile Supports for Diverse Nanofibers and Their Applications in Environmental Sensing, *Adv. Fiber Mater.*, 2023, **5**, 429–460.
10 P. Fattahi, J. Dover and J. Brown, 3D Near-Field Electrospinning of Biomaterial Microfibers with Potential for Blended Microfiber-Cell-Loaded Gel Composite Structures, *Adv. Healthcare Mater.*, 2017, **6**, 1700456.
11 J. Song, M. Kim and H. Lee, Recent advances on nanofiber fabrications: Unconventional state-of-the-art spinning techniques, *Polymers*, 2020, **12**, 1386.
12 J. Zhou, X. Li, Z. Zhang, T. Hou, J. Xu, Y. Wang, H. Ye and B. Yang, Bio-based and bio-degradable nanofiber materials: A sustainable platform for energy, environmental, and biomedical applications, *Chem. Eng. J.*, 2024, **491**, 152105.
13 R. Kumar, R. Singh, M. Singh and P. Kumar, On ZnO nano particle reinforced PVDF composite materials for 3D printing of biomedical sensors, *J. Manuf. Process.*, 2020, **60**, 268–282.
14 H. Eng, S. Maleksaeedi, S. Yu, Y. Y. C. Choong, F. E. Wiria, C. L. C. Tan, P. C. Su and J. Wei, 3D Stereolithography of Polymer Composites Reinforced with Orientated Nanoclay, *Procedia Eng.*, 2017, **216**, 1–7.
15 C. Liao, A. Wuethrich and M. Trau, A material odyssey for 3D nano/microstructures: two photon polymerization based nanolithography in bioapplications, *Appl. Mater. Today*, 2020, **19**, 100635.
16 H. Kim, F. Torres, Y. Wu, D. Villagran, Y. Lin and T.-L. Tseng, Integrated 3D printing and corona poling process of PVDF piezoelectric films for pressure sensor application, *Smart Mater. Struct.*, 2017, **26**, 085027.
17 S. Bodkhe, P. S. M. Rajesh, F. P. Gosselin and D. Therriault, Simultaneous 3D Printing and Poling of PVDF and Its Nanocomposites, *ACS Appl. Energy Mater.*, 2018, **1**, 2474–2482.
18 J. Fan, N. Deneke, S. Xu, B. Newell, J. Garcia, C. Davis, W. Wu, R. M. Voyles and R. A. Nawrocki, Electric poling-assisted additive manufacturing technique for piezoelectric active poly(vinylidene fluoride) films: Towards fully three-dimensional printed functional materials, *Addit. Manuf.*, 2022, **60**, 103248.
19 K. C. Chan, A. Sadaf, J. Gerrit Korvink and W. Wenzel, Electromechanical analysis of electrospun polymer fiber deposition, *J. Appl. Phys.*, 2023, **134**, 184902.
20 M. M. Nazemi, A. Khodabandeh and A. Hadjizadeh, Near-Field Electrospinning: Crucial Parameters, Challenges, and Applications, *ACS Appl. Bio Mater.*, 2022, **5**, 394–412.
21 X. Li, Z. Li, L. Wang, G. Ma, F. Meng, R. H. Pritchard, E. L. Gill, Y. Liu and Y. Y. S. Huang, Low-Voltage Continuous Electrospinning Patterning, *ACS Appl. Mater. Interfaces*, 2016, **8**, 32120–32131.
22 Y. Huang, Y. Li, Y. Zhang, H. Yu and Z. Tan, Near-field electrospinning for 2D and 3D structuring: Fundamentals, methods, and applications, *Mater. Today Adv.*, 2024, **21**, 100461.
23 E. Cortés, C. Molina, L. Rodriguez-Lorenzo and N. Cubo Mateo, Generation of Controlled Micrometric Fibers inside Printed Scaffolds Using Standard FDM 3D Printers, *Polymers*, 2022, **15**, 96.
24 M. Calzado-Delgado, M. O. Guerrero-Pérez and K. L. Yeung, A new versatile x–y–z electrospinning equipment for nanofiber synthesis in both far and near field, *Sci. Rep.*, 2022, **12**, 4872.
25 D. G. Dassanayaka, T. M. Alves, N. D. Wanasekara, I. G. Dharmasena and J. Ventura, Recent Progresses in Wearable Triboelectric Nanogenerators, *Adv. Funct. Mater.*, 2022, **32**, 2205438.
26 D. Shin, J. Kim and J. Chang, Controlled initiation and termination of jetting in near-field electrospinning through voltage-driven surface charge manipulation, *J. Manuf. Process.*, 2023, **90**, 226–232.
27 J. Wiegmann, C. Leppin, A. Langhoff, J. Schwaderer, S. Beuermann, D. Johannsmann and A. P. Weber, Influence of the solvent evaporation rate on the β-Phase content of electrosprayed PVDF particles and films studied by a fast Multi-Overtone QCM, *Adv. Powder Technol.*, 2022, **33**, 103452.
28 D. L. Chinaglia, R. Gregorio Jr., J. C. Stefanello, R. A. Pisani Altafim, W. Wirges, F. Wang and R. Gerhard, Influence of the solvent evaporation rate on the crystalline phases of solution-cast poly(vinylidene fluoride) films, *J. Appl. Polym. Sci.*, 2010, **116**, 785–791.
29 S. Bodkhe, G. Turcot, F. P. Gosselin and D. Therriault, One-Step Solvent Evaporation-Assisted 3D Printing of Piezoelectric PVDF Nanocomposite Structures, *ACS Appl. Mater. Interfaces*, 2017, **9**, 20833–20842.
30 G. Taguchi and M. S. Phadke, in *Quality Control, Robust Design, and the Taguchi Method*, ed. K. Dehnad, Springer US, Boston, MA, 1989, pp. 77–96.
31 M. Hikmat, S. Rostam and Y. M. Ahmed, Investigation of tensile property-based Taguchi method of PLA parts fabricated by FDM 3D printing technology, *Results Eng.*, 2021, **11**, 100264.
32 I. Mardiono, Y.-C. Wang, I. E. Saputro, L.-R. Huang, W.-Y. Chang, S.-K. Lu, H.-H. Chang, T.-S. Shih and Y.-K. Fuh, Multi-response optimization of processing parameters and stack configuration for enhanced mechanical properties of high-strength carbon fiber composite, *Int. J. Adv. Des. Manuf. Technol.*, 2025, **140**, 2575–2593.
33 A. R. Nuranto, A. Nurrohmad, A. Nugroho, D. Hidayat, A. J. Fitroh, F. C. Megawanto, Chairunnisa, A. B. Utama and F. Imaduddin, Experimental and statistical optimization of FDM 3D printing parameters for improved surface roughness and specific bending load, *J. Mech. Sci. Technol.*, 2025, **39**, 5073–5082.
34 K. R. Kaja, S. A. Behera, B. Das, S. Hajra, S. Panda, M. A. Belal, N. Vittayakorn, B. Nanda, P. G. R. Achary and H. J. Kim, Calcium Copper Titanate Particles Based Energy Harvesting and Removal of Pharmaceutical Pollutants, *ACS Appl. Electron. Mater.*, 2025, **7**, 4327–4338.
35 N. Mridha, C. M. Nannapaneni, M. H. Shaikh, S. Pratihar, A. Yella and P. K. S. Mural, Photo-Assisted Energy Harvesters and Sensors Using PVDF Matrix-Stabilized α-FAPbI3 Perovskite with AI/ML-Based Human Kinematic Detection, *ACS Appl. Electron. Mater.*, 2026, **8**, 1320–1337.

36 K. R. Kaja, S. Hajra, S. Panda, M. Belal, S. Nam, P. Pakawanit, B. K. Panigrahi, H. Khanbareh, C. Bowen, J. Yu and H. J. Kim, Waste polyethylene-coated fabrics for dual-mode interfaces triboelectrification for self-powered sensors, *Results Eng.*, 2025, **28**, 107111.

37 S. Hajra, S. Panda, K. R. Kaja, M. A. Belal, V. Vivekananthan and H. J. Kim, Self-Powered Fire Safety Indicator Based on Fabric-Based Triboelectric Nanogenerator, *Energy Technol.*, 2025, **13**, 2402488.

38 L. Zhao, Y. Xia, R. Hebibul, J. Wang, X. Zhou, Y. Hu, Z. Li, G. Luo, Y. Zhao and Z. Jiang, Evaluation of width and width uniformity of near-field electrospinning printed micro and sub-micrometer lines based on optical image processing, *J. Micromech. Microeng.*, 2018, **28**, 035010.

39 A. Haider, S. Haider and I.-K. Kang, A comprehensive review summarizing the effect of electrospinning parameters and potential applications of nanofibers in biomedical and biotechnology, *Arabian J. Chem.*, 2018, **11**, 1165–1188.

40 D. Sun, C. Chang, S. Li and L. Lin, Near-Field Electrospinning, *Nano Lett.*, 2006, **6**, 839–842.

41 Ö. Verim, O. Saeed, M. H. Eid, S. F. Mahmoud, D. I. Saleh and A. E. Elwakeel, Investigation of the effects of 3D printing parameters on mechanical tests of PLA parts produced by MEX 3D printing using Taguchi method, *Sci. Rep.*, 2025, **15**, 15008.

42 N. Sayyar, W. M. Tucho, E. Undheim and V. Hansen, Adaptive Control of Additive Manufacturing Parameters in Pulsed Laser-Based Directed Energy Deposition of Super Duplex Stainless Steel: Hybrid Taguchi-Grey Relational Approach, *Met. Mater. Int.*, 2026, **32**, 195–229.

43 Wahyudin, A. Kharisma, R. D. J. Murphiyanto, M. K. Perdana and T. P. Kasih, Application of Taguchi method and ANOVA in the optimization of dyeing process on cotton knit fabric to reduce re-dyeing process, *IOP Conf. Ser. Earth Environ. Sci.*, 2017, **109**, 012023.

44 S. Pratihar, A. M. Chandran, N. Mridha, A. Yella and P. K. S. Mural, Tunable Self-Poled 2D h-BN/PVDF Nanofibers for Enhanced Electromechanical and Electrochemical Applications, *ACS Appl. Electron. Mater.*, 2025, **7**, 2751–2766.

45 N. Mridha, M. Garg, S. Pratihar, K. Bulia, M. H. Shaikh, A. Yella and P. K. S. Mural, Enhanced piezoelectric performance of PAN nanofibers incorporated with a lead-free high entropy perovskite oxide for energy harvesting, sensing and IoT-based smart alert systems for security monitoring, *J. Mater. Chem. C*, 2026, **14**, 5764–5782.

46 A. Aishwarya, A. Naskar, T. Dasgupta and A. R. Bhattacharyya, Mono-lithium salt of adipic acid exfoliated molybdenum sulphide incorporated poly(vinylidene fluoride) nanocomposites with enhanced piezoelectric properties for energy harvesting and dye degradation, *J. Alloys Compd.*, 2025, **1036**, 182155.

47 A. Wang, C. Chen, L. Liao, J. Qian, F.-G. Yuan and N. Zhang, Enhanced β-Phase in Direct Ink Writing PVDF Thin Films by Intercalation of Graphene, *J. Inorg. Organomet. Polym. Mater.*, 2020, **30**, 1497–1502.

48 M. Singh, B. C. Yadav, A. Ranjan, M. Kaur and S. K. Gupta, Synthesis and characterization of perovskite barium titanate thin film and its application as LPG sensor, *Sens. Actuators, B*, 2017, **241**, 1170–1178.

49 M. R. Atta, N. Algethami, M. O. Farea, Q. A. Alsulami and A. Rajeh, Enhancing the structural, thermal, and dielectric properties of the polymer nanocomposites based on polymer blend and barium titanate nanoparticles for application in energy storage, *Int. J. Energy Res.*, 2022, **46**, 8020–8029.

50 B. Jiang, J. Iocozzia, L. Zhao, H. Zhang, Y.-W. Harn, Y. Chen and Z. Lin, Barium titanate at the nanoscale: controlled synthesis and dielectric and ferroelectric properties, *Chem. Soc. Rev.*, 2019, **48**, 1194–1228.

51 S. Mahboubizadeh, S. T. Dilamani and S. Baghshahi, Piezoelectricity performance and β-phase analysis of PVDF composite fibers with BaTiO3 and PZT reinforcement, *Heliyon*, 2024, **10**, e25021.

52 M. Yasar, P. Hassett, N. Murphy and A. Ivankovic, β Phase Optimization of Solvent Cast PVDF as a Function of the Processing Method and Additive Content, *ACS Omega*, 2024, **9**, 26020–26029.

53 K. Kukreja, S. Pratihar, P. K. Panda and P. K. S. Mural, High-performance piezoelectric nanogenerator based on PVDF/2D layered Mo_3AlC_2 composites for sustainable energy harvesting applications, *Sens. Actuators, A*, 2026, **399**, 117415.

54 E. Tarani, I. Arvanitidis, D. Christofilos, D. N. Bikiaris, K. Chrissafis and G. Vourlias, Calculation of the degree of crystallinity of HDPE/GNPs nanocomposites by using various experimental techniques: a comparative study, *J. Mater. Sci.*, 2023, **58**, 1621–1639.

55 M. Fatema, A. Bajpai, A. Somvanshi, S. Manzoor, M. Arshad, N. Zarrin, A. A. A. Qahtan, W. Khan and S. Husain, Study of structural correlations with temperature dependent dielectric response and ferroelectric behavior for (Sr, Mn) co-doped BaTiO3, *J. Mater. Sci.: Mater. Electron.*, 2022, **33**, 6329–6353.

56 M. Singh, B. C. Yadav, A. Ranjan, M. Kaur and S. K. Gupta, Synthesis and characterization of perovskite barium titanate thin film and its application as LPG sensor, *Sens. Actuators, B*, 2017, **241**, 1170–1178.

57 A. S. Jayasekara and P. Cebe, Quantitative analysis of polar crystalline fractions in poly(vinylidene fluoride) electrospun fibers and electrosprayed films, *Polymer*, 2023, **281**, 126140.

58 X. Cai, T. Lei, D. Sun and L. Lin, A critical analysis of the α, β and γ phases in poly(vinylidene fluoride) using FTIR, *RSC Adv.*, 2017, **7**, 15382–15389.

59 I. Coondoo, V. B. Isfahani, H. Amorín, I. Bdikin, J. Carvalho, C. Pascual-González, B. M. Silva, J. Oliveira, D. Pukazhselvan, B. G. Almeida and G. Miranda, Flexible and multifunctional P(VDF-TrFE)/BT-BMT polymer composite films: Realizing high piezoelectric performance and electrocaloric effect, *Chem. Eng. J.*, 2025, **505**, 158639.

60 L. Gong, Y. Hao, H. Liu, B. Xi, Y. Cao and Y. Cao, Enhancement of α to β phase transformation in poly (vinylidene fluoride) nanocomposites under uni-axial stretch: Contribution from restriction of nano-particles, *Polym. Test.*, 2024, **138**, 108516.

61 H. Kim, F. Torres, D. Villagran, C. Stewart, Y. Lin and T.-L. B. Tseng, 3D Printing of BaTiO3/PVDF Composites with Electric In Situ Poling for Pressure Sensor Applications, *Macromol. Mater. Eng.*, 2017, **302**, 1700229.

62 A. A. Ribeiro, R. F. C. Marques, A. C. Guastaldi and J. S. de Carvalho Campos, Hydroxyapatite deposition study through polymeric process on commercially pure Ti surfaces modified by laser beam irradiation, *J. Mater. Sci.*, 2009, **44**, 4056–4061.

63 J. Zhou, L. Xu, L. Zhang, J. Zhang and A. Zhang, Electrospun Polyvinylidene Fluoride Nanogenerator with Hydrophobic Properties and Enhanced Energy Harvesting for Wearable and Wireless Sensing, *ACS Appl. Electron. Mater.*, 2024, **6**, 2026–2038.

64 D. Kanmaz, R. Celen, E. Karaca and G. Manasoglu, Investigation of Wettability, Thermal Stability, and Solar Behavior of Composite Films Based on Thermoplastic Polyurethane and Barium Titanate Nanoparticles, *Polymers*, 2024, **16**, 3259.

65 J.-H. Zhang and X. Hao, Enhancing output performances and output retention rates of triboelectric nanogenerators via a design of composite inner-layers with coupling effect and self-assembled outer-layers with superhydrophobicity, *Nano Energy*, 2020, **76**, 105074.

66 H. Parangusan, D. Al-Sowaidi, E. H. Elhadrami, D. Ponnamma and J. Bhadra, Development of flexible PVDF/BaTiO3-MoS2 polymer nanocomposites for energy harvesting and gas sensing applications, *J. Mater. Sci.: Mater. Electron.*, 2024, **35**, 679.

67 S. Pratihar, A. M. Chandran, A. R. Bhat and P. K. S. Mural, Piezoelectric Nanogenerators Based on Poly(vinylidene fluoride) Doped with High Entropy Oxide Nanoparticles for Sensitive Pressure Sensors, *ACS Appl. Nano Mater.*, 2024, **7**, 20553–20568.

68 M. S. Kwak, Y.-J. Park, M. P. Kim and H. Ko, Interfacial Polarization for High-Performance Triboelectric Devices: Principles, Strategies, and Applications, *ACS Appl. Mater. Interfaces*, 2025, **17**, 37336–37352.

69 Z. Liwei, S. Na, W. Xuan, W. Liqiu, C. Haikuo and J. Tianyuan, Analysis on dielectric loss characteristics of polyvinylidene fluoride and its composites, *J. Mater. Sci.: Mater. Electron.*, 2021, **32**, 26268–26290.

70 H. Wang, Z.-Y. Zhao, M.-H. Lin, X.-F. Wu, G. Yu, S.-L. Lin, J.-C. Wang and E.-P. Zhou, Enhancement of Dielectric Energy Storage of PVDF-Based Composites With 2D Sheet-Like MOFs, *Polym. Compos.*, 2025, **46**, 14251–14261.

71 K. Sreejivungsa and P. Thongbai, Enhanced dielectric properties of PVDF polymer nanocomposites: A study on gold–decorated, surface–modified multiwalled carbon nanotubes, *Heliyon*, 2024, **10**, e26693.

72 T. Aravinda, S. Rao, V. Kumbla and J. Pattar, Improved dielectric performance of polyvinylidene fluoride (PVDF) – Carbon dots composites, *Phys. E*, 2023, **147**, 115589.

73 C. Zhu, K. Li, X. Liu, Y. Li, J. Yin, L. Hong and Q. Qin, Enhanced Dielectric Performance in PVDF-Based Composites by Introducing a Transition Interface, *Polymers*, 2025, **17**, 137.

74 A. Aishwarya, S. Mondal, N. Bhattacharjee, T. Dasgupta and A. R. Bhattacharyya, Molybdenum sulphide incorporated flexible poly(vinylidene fluoride) nanocomposites for energy harvesting and water remediation by dye degradation via piezocatalysis, *Polym. Compos.*, 2025, **46**, 8533–8555.

75 J. H. Kim, J. Jeong, D. S. Kong, H. Yoon, H. Cho, J. H. Jung and J. Y. Park, Direct Observation of Contact Electrification Effects at Nanoscale Using Scanning Probe Microscopy, *Adv. Mater. Interfaces*, 2024, **11**, 2300821.

76 Q.-Z. Guo, L.-C. Yang, R.-C. Wang and C.-P. Liu, Tunable Work Function of MgxZn1–xO as a Viable Friction Material for a Triboelectric Nanogenerator, *ACS Appl. Mater. Interfaces*, 2019, **11**, 1420–1425.

77 J. Ye, T. Xu, L. Germane, L. Lapcinskis, A. Šutka and J.-C. Tan, Functionalized PDMS for regulating the triboelectric output of nanogenerators: a study of charge transfer mechanisms, *J. Mater. Chem. C*, 2025, **13**, 7654–7663.

78 A. Mahapatra, D. Deepak, T. Singh, K. Agarwal and S. S. Roy, Fluorinated-PDMS enhanced single-electrode triboelectric nanogenerator for biomechanical energy harvesting and sensing applications, *APL Electron. Devices*, 2026, **2**, 016121.

79 M. S. Ravisankar, K. Pramod and R. B. Gangineni, Effect of the top electrode on local piezoelectric and the ferroelectric response of PVDF thin films in PVDF/Au/Si and Ag/PVDF/Au/Si multilayers, *Appl. Phys. A: Mater. Sci. Process.*, 2023, **129**, 146.

80 M. Y. Chougale, Q. M. Saqib, M. U. Khan, R. A. Shaukat, J. Kim and J. Bae, Novel Recycled Triboelectric Nanogenerator Based on Polymer-Coated Trash Soda Can for Clean Energy Harvesting, *Adv. Sustainable Syst.*, 2021, **5**, 2100161.

81 J. Du, Z. Liu, H. Luo, S. Li, X. Tao, L. Zheng, D. Yang and X. Chen, Tunable polarity reversal phenomenon at the initial working state of triboelectric nanogenerator, *Nano Energy*, 2022, **102**, 107651.

82 A. R. Bhat, V. N. Sasi, S. Pratihar, A. M. Chandran and P. K. S. Mural, Signal Generation Mechanisms with Isolated and Characterized Piezo/Tribo Signals for Precise Energy Harvesting Analysis: A Pathway to Integrated Hybrid Nanogenerator Fabrication, *ACS Appl. Energy Mater.*, 2025, **8**, 6528–6544.

83 A. M. Chandran, S. Varun and P. K. S. Mural, Flexible electroactive PVDF/ZnO nanocomposite with high output power and current density, *Polym. Eng. Sci.*, 2021, **61**, 1829–1841.

84 C. Chang, V. H. Tran, J. Wang, Y. K. Fuh and L. Lin, Direct-write piezoelectric polymeric nanogenerator with high energy conversion efficiency, *Nano Lett.*, 2010, **10**, 726–731.

85 S. Xu, X. Fu, G. Liu, T. Tong, T. Bu, Z. L. Wang and C. Zhang, Comparison of applied torque and energy conversion efficiency between rotational triboelectric nanogenerator and electromagnetic generator, *iScience*, 2021, **24**, 102318.